ABSTRACT

BROWN, PATRICK. A Three-Dimensional Multi-Resolution Admittance Method for Low-Frequency Bioelectromagnetic Interaction . (Under the direction of Dr. Gianluca Lazzi.)

A three-dimensional multi-resolution admittance method has been developed, tested, and shown to be capable of reducing computational cell counts by over 50% while maintaining a high level of accuracy. The method was used to investigate the properties of retinal prosthesis electrode configurations situated in anatomically realistic models of the ocular orbit. These simulations indicated that the epi-retinal electrode array which places the electrodes against the retinal surface is a viable candidate for precise ganglion cell stimulation. The trans-retinal electrode array, in which the electrodes were placed outside of the eye, against the sclera, was shown to not be a suitable solution.

Two-dimensional simulations were used to determine current spread characteristics of coaxial electrodes in a high-resolution retinal model. As total electrode width was increased, a gradual transition from a quadratic to linear relationship between current density induced in the ganglion cell layer and electrode size was observed. Furthermore, two-dimensional simulations were used to estimate the influence of imperfect retina-electrode contact for epi-retinal electrodes by placing a conductive channel between the two surfaces. The general shape of the current patterns was found to be similar, but the current densities were reduced between 0-27% in the model with the conductive gap.

A Three-Dimensional Multi-Resolution Admittance Method for Low-Frequency Bioelectromagnetic Interaction

by

Patrick K. Brown

A thesis submitted to the Graduate Faculty of
North Carolina State University
in partial satisfaction of the
requirements for the Degree of
Master of Science

Electrical Engineering

Raleigh, NC

2005

Approved By:

Dr. Douglas Barlage

Dr. Griff Bilbro

Dr. Gianluca Lazzi
Chair of Advisory Committee

Biography

Patrick Brown was born in Beaumont, Texas, but spent most of his life in Asheville, North Carolina. He received the Bachelor of Science degree in Electrical Engineering from North Carolina State University in 2002, graduating as Valedictorian of his class. His research interests include the development of novel computational methods for modeling the electrical characteristics of biological tissues.

Acknowledgements

I would like to thank my advisor, Dr. Gianluca Lazzi, for giving me the opportunity to participate in his research group. Working with Dr. Lazzi and his team of excellent graduate students has been a challenging and rewarding experience.

I would like to thank Michael Eberdt, whose work laid the foundation for my own. Without his tireless help, especially in the early stages, this thesis would not have been possible.

I would like to thank the students in Dr. Lazzi's lab who either helped me with my work specifically or else simply made working around the lab more fun: Abheek Gupta, Anand Konanur, Ajit Rajagopalan, Guarav Gupta, Stefan Schmidt, Shruthi Soora, Vinit Singh, and Keyoor Gosalia. In particular, I would like to thank Carlos Cela who is continuing the work with the Admittance Method. The project passed into his very capable hands, and I am excited to see where he takes it.

Finally, I would like to thank my family and friends for their understanding and support during the time I was pursing this degree. Without them this would not have been possible.

Contents

List of Figures

List of Tables

Chapter 1

Introduction

The field of artificial, electrical neural stimulation has rapidly expanded in recent years. This progress is likely due to both an increase in the understanding of the way to the nervous system operates, and to the explosion of specialized integrated circuit technology. Artificial neural stimulation techniques can be used to induce neural activity by electrically stimulating nerves in ways to compensate for lost functionality of injured nervous tissues. Neural prostheses have been developed to aid in the stimulation of muscles and the treatment of pain. [1] Furthermore, artificial neural stimulation has been implemented both in the most peripheral areas of the nervous system such as sensory organs and at some of the deepest, most central parts of the nervous system such as the spinal cord and cerebral cortex.

The cochlear implant stands as a notable achievement in the field of artificial neural stimulation. The cochlea is the spiraled, conch-shell shaped organ of the inner ear that transduces the mechanical pressure waves of sound into a chemical-electrical neural signal. Used by over 20,000 people world-wide the cochlear implant can restore a limited auditory

sense to patients suffering from severe hearing loss. [2] The implant was designed to use the malfunctioning cochlea of the hearing impaired as a way to map artificial sensory input into the nervous system. Using the fact that different regions of the cochlea are responsible for sounds of differing frequencies, the implant selectively stimulates the appropriate regions of the cochlea to create sensations of sound.

In the same spirit as the cochlear implant, there has been much work toward visual prostheses to restore a partial form of vision in patients suffering from acquired blindness due to retinal degenerative diseases. The retina is the thin layer of nervous tissue lining the back of the eye that transduces light into neural signals. It is the light sensitive retinal photoreceptor cells become non-functional in these diseases. The effort to build a visual prosthesis, although in some ways similar in principle to the cochlear implant, provides a different set of challenges because of the differing structures of the sensory organs. In visual prostheses, injection of electrical currents into the retinal tissue is one possible means of providing a sensory input. To provide intelligible information, these electrical currents must precisely stimulate only desired regions of the retinal tissue. This requires control of the current spread patterns in the retina so that current densities are high in regions we wish to stimulate, but low in regions we do not with to stimulate. In order to meet this objective, it would be advantageous if an electrode array could be designed specifically to meet this requirement. Therefore, to aid in this design process, a multi-resolution admittance method has been created to simulate the retinal current patterns that would be induced by various electrode shapes and configurations.

In the remainder of this first chapter the background necessary to properly explain electrical stimulation of neural tissue is presented. Then, a summary of the problems a

retinal prosthesis seeks to address is described followed by a brief account of admittance method simulation schemes.

1.1 Basics of Cell Membranes

Cell membranes separate the internal environment of a cell from the surrounding medium. The selective movement of metabolites across the cell membrane is one of the most fundamental defining attributes in living organisms. [3] Because understanding the nature of cell membranes is fundamental to understanding the working principles of the retinal prosthesis, the structure and properties of cell membranes are briefly covered.

1.1.1 Dipolar Nature of Water

Water molecules exhibit a dipolar charge characteristic. This characteristic results from the asymmetry of the water molecule. Oxygen has six outer orbital electrons, two of these are shared in covalent bonds with hydrogen atoms. The remaining four electrons form nonbonded pairs. Due to the tetrahedral shape visible in Figure 1.1, the charge distribution is not symmetric, leading the dipolar characteristic. The ultimate result is a slight negative charge around the oxygen and an electron deficiency around the hydrogen atoms. The result is the dipolar characteristic of water shown in Figure 1.1.

The oxygen in water molecules has strong electron drawing tendencies, causing the negatively charged electrons in the bonds to tend to shift towards the oxygen nucleus and away from the hydrogen nuclei. Temporary bonds called *hydrogen bonds* can the be formed between the negatively charged oxygen atom of one molecule and a positively

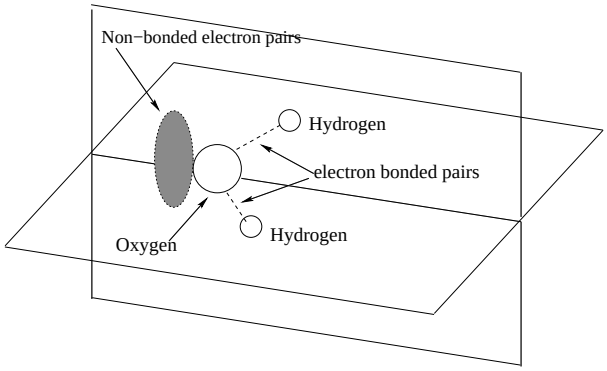

Figure 1.1: Dipolar structure of water. The non-bonded electrons of the oxygen atom create an unbalanced charge characteristic.

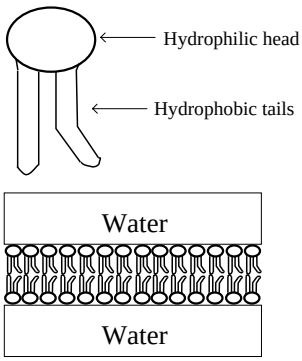

Figure 1.2: Top: Phospholipid structure Bottom: Phospholipid bilayer structure. The hydrophopic regions are isolated from water.

charged hydrogen of an adjacent water molecule. This tendency of water to be attracted to the electrical charges of other water molecules can be generalized to other charged species such as ions and charged organic molecules, and is the reason ionic compounds such as NaCl (table salt) are highly soluble in water. These types of materials are termed *hydrophilic*, or water loving. Non-ionic, non-charged species, however, are not attacked by water. Rather, water molecules tend to form hydrogen bonds among themselves to the exclusion of the non-charged agents, explaining why non-charged species such as organic oils are highly water-insoluble. These types of materials are referred to as *hydrophobic*, or water fearing.

1.1.2 Phospholipids and Bilayers

A special type of molecule, known as a phospholipid, consists of a hydrophilic head connected to two long hydrophobic tails as shown in Figure 1.2. When many of these molecules are mixed with water, the phospholipids are arranged into structures that allow the hydrophilic heads to interact with water, but shield the hydrophobic tails. One of these structures, the phospolipid bilayer, is the fundamental structure of cell membranes.

As shown in Figure 1.2, the lipid bilayer isolates the hydrophobic tails from water molecules. Because of the hydrophobic region embedded within the layer, charged species cannot easily cross the lipid bilayer. Non-charged molecules, however, could cross the boundary more easily.

1.1.3 Selective Permeability of Membranes

The phospholipid bilayers that form cell membranes restrict the passage charged ion species. However, some of these types of molecules do cross the membrane. This selective permeability is partially due to proteins embedded in the lipid bilayer. These special types of transport proteins span the entire width of the membrane and can create channels to selectively facilitate the passage of materials that otherwise would be less able to pass through the membrane.

Protein mediated transport occurs both as a passive process, requiring no input of energy, and as an active process, requiring energy. Many physiological processes create potential energy by using active ion transport to form ion gradients across membranes. Then the ions are allowed to diffuse back down the gradient in an energy releasing process

via other transporter proteins. These proteins can use the released energy to perform useful work, often by either forming or breaking chemical bonds.

1.1.4 Trans-Membrane Potentials

When the net charge density on one side of a membrane differs from that of the other, an electric field is created across the membrane resulting in a trans-membrane potential. This potential is calculated by the Goldman equation (1.1.1). In this equation each ion species has an affiliated membrane permeability p that is unique to that particular species. This equation would be applied in a case where there are n cation species and m anion species. The subscripts i and o indicate concentrations on the inside and outside of an enclosed cell membrane respectively.

$$V_m = \frac{-RT}{F} ln \frac{\sum_{x=1}^{n}[p_c[C^+]_o]_x + \sum_{y=1}^{m}[p_a[A^-]_i]_y}{\sum_{x=1}^{n}[p_c[C^+]_i]_x + \sum_{y=1}^{m}[p_a[A^-]_o]_y} \, mV \tag{1.1.1}$$

R	8.314 J/K mole
F	96,487 coulombs/mole
T	Temperature (K)
p	ion permeability

1.1.5 Neurons and Action Potentials

Neural behavior can be partially characterized by fluctuations of voltage potentials across the neural cell membrane. In its resting state, a typical neuron (a single nerve cell) maintains an ion gradient that results in approximately a -65 mV potential. This resting potential is maintained primarily by K^+ and Na^+ gradients across the membrane. While the membrane is slightly porous to these ions, allowing a slow leakage across the membrane, active transport protein pumps continuously work to maintain the gradient.

Other transport proteins embedded in the neural cell membrane are gated ion channels specialized to K^+, Na^+, and Ca^{2+}. When appropriately stimulated, these channels selectively allow the flow of ions across the membrane. These channels generally respond to one of two kinds of stimuli, either chemical or electrical. The chemically activated ion channels respond to special neurotransmitter molecules that are typically released from adjacent neurons, whereas the electrically activated channels respond to changes in trans-membrane potential. These two types of ion channels function jointly to produce the action potential activity seen in neurons.

Chemically stimulated ion channels respond to neurotransmitters. When an excitatory neurotransmitter binds momentarily to an ion channel, the channel opens, allowing the passage of ions, slightly reducing the trans-membrane potential. The number of channels activated, and the duration during which they are open corresponds to the concentration of neurotransmitter present. Therefore, if neurotransmitter is present only in small quantities, ion channels will not be strongly activated, resulting in little net voltage potential change. Conversely, when present in large quantities, the net voltage can change significantly. In this way, the electrical potential of the neuron responds in a graded manner to the chemical stimulus.

When neurotransmitters are present in sufficient quantities to raise the transmembrane potentials from -65 mV to approximately -50 mV, the second type of ion channel, voltage gated ion channels, are activated. When these channels open, the resulting ion flow further dissipates the membrane potential (making it less negative.) This membrane potential change can activate the surrounding voltage gated channels resulting in a chain reaction that propagates down the length of the neuron. This electrical chain reaction

is termed an "action potential" and is a threshold, all-or-nothing type response with the ultimate result of releasing neurotransmitters from the axon terminal. These neurotransmitters may then stimulate adjacent neurons to perpetuate the process. The cumulative effect of many intricately interconnected neurons interacting in this way is a fundamental concept of nervous system function.

1.1.6 Artificial Neural Stimulation

In the event that neurons fail to function properly, or are inadequately stimulated, an artificial electrical stimulus can partially substitute for the natural chemical neural stimulation by placing electrodes in close proximity to the dysfunctional neural tissue. These electrodes induce neural activity by forcing a change in voltage potential along the neurons. It has been shown with the cochlear implant that transmembrane potentials can be manipulated by applying an electric field and that these changes can be interpreted as sensory information [4].

1.2 Visual Neurology

Sensory organs all contain sensory receptors which are specialized neural tissue that is excited by external sensory stimuli rather than by the chemical neurotransmitters of other neurons. The retina is the neural tissue in the back of the eye responsible for transducing visual stimuli into a neural signal. It is a thin, multi-layered structure ranging in thickness from approximately 250-450 μm [5] and consisting of multiples kinds of specialized cells. Light sensitive pigment molecules in photoreceptor cells initiate an

electrical and chemical signaling process. Then the bipolar, amacrine, and horizontal cells process this signal through a series of complex interactions. Finally the Ganglion Cell Layer (GCL) is stimulated and the optic nerve (which consists of the ganglion cell axons) carries the visual signal from the eyeball to the brain centers [6].

1.3 Retina Degeneration

The retinal degenerative diseases Age Related Macular Degeneration (AMD) and Retinis Pigmentosa (RP) cause the degradation and eventual death of the light sensing photoreceptor cells in the retina, leading to a gradual loss of vision, and eventual blindness. However, while the photoreceptor cells become inoperative, the rest of the visual pathway remains functional. Humayun et al. demonstrated that visual sensation could be produced in patients with advanced AMD and RP by stimulating the retina with fine tipped probe electrodes. [7] The perceived bursts of light seen in the patients' visual fields result from the stimulation of the ganglion cell layer located beneath the retinal surface. Because the ganglion cell layer passes information from the photoreceptor cells to the optic nerve, stimulating the ganglion cells with an electrical current can serve as a means of bypassing the non-functional photoreceptor cells.

1.4 NCSU/USC Retinal Prosthesis System

1.4.1 Overview

In the late 1980's, researchers at Johns Hopkins University (since relocated to the University of Southern California) in conjunction with North Carolina State University began investigating the possibility of using artificial retinal stimulation as a treatment for advanced retinal degenerative diseases. The retinal prosthesis system eventually proposed is shown in Figure 1.3. In this system, active electronic circuitry is used to provide the current stimulus, meaning that a small microprocessor is actually implanted within the eye. It is proposed that power will be delivered to the prosthetic chip by means of a wireless inductive link, and a separate data link will deliver visual information. A camera, ideally resting on a set of glasses in front of the eye, will provide the visual image. The prosthesis uses a grid of electrodes, placed on the retina surface, to systematically stimulate the ganglion cell layer so that a meaningful visual sensation is created.

1.4.2 Electrode Requirements for Retinal Prosthesis

For a retinal prosthesis to operate effectively, each electrode in the array should stimulate only the area of the retina within a close proximity. Specifically, a current from one electrode should not be able to stimulate the retinal cells beneath an adjacent electrode. The ganglion cells stimulated should fall in the same spatial pattern as that of the firing electrodes. Meeting this requirement can be problematic because there must be a current return path back to the prosthesis. Furthermore, the current path is largely a function of the retina's anatomical structure. Therefore, the anatomy of the eye

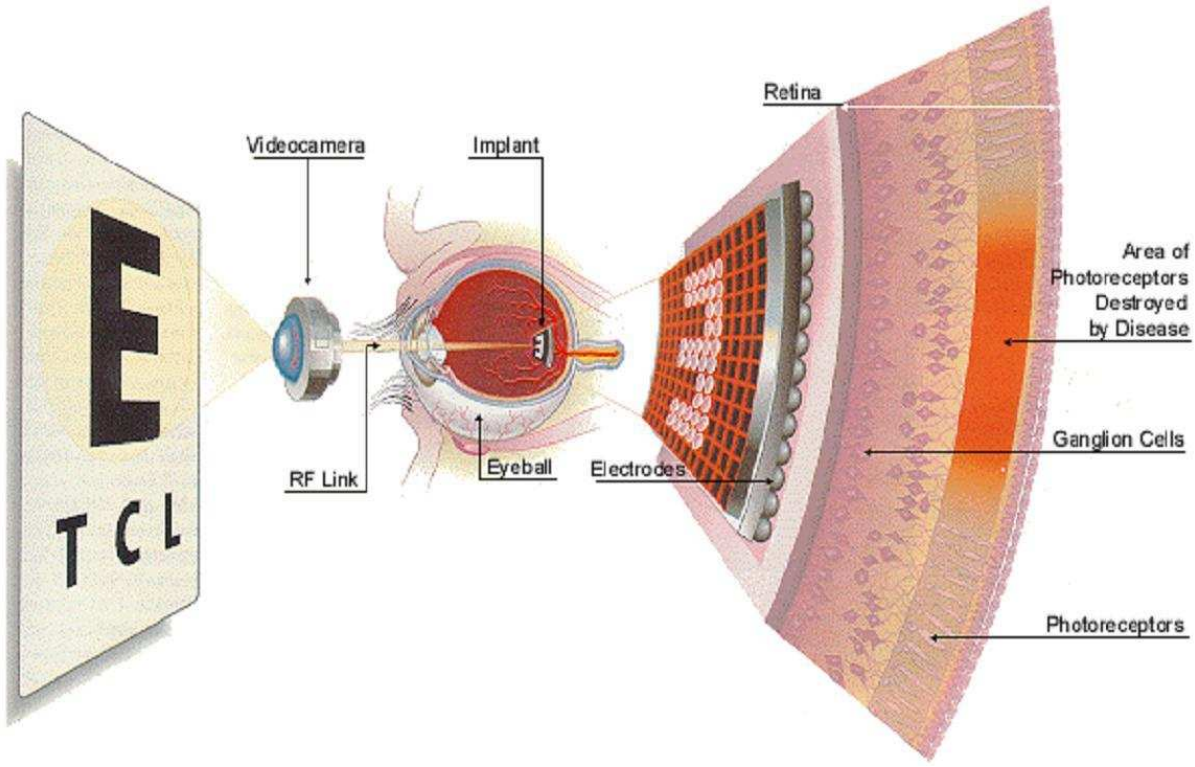

Figure 1.3: Proposed NCSU/USC retinal prosthesis system.

and retina must be considered when designing the electrode array such that the current distribution can be controlled.

Safety is also a consideration for electrode design. Excessive power dissipation in human tissue has the potential to cause severe damage, especially in delicate nervous tissues such as that found in the retina. If current could be directed only where needed then the total current injected into the retina could be minimized. Also, from an operational standpoint, the retinal prosthesis system will consume less power if the injected current is minimized.

To stimulate the retina precisely (localize the current path to a small area around each electrode) and efficiently (with minimal power consumption) a simulation method

is needed that will allow the design and testing of different types of electrode arrays. The natural electrical activity of neural tissue has been the subject of much study and has been characterized at the cellular [11] and integrative levels. [12] While these methods accurately model electrical activity of individual neurons, in biomedical applications such as the retinal prosthesis a more general, macroscopic, simulation method is required. Specifically, the current densities in tissues exposed to external electrical stimuli such as magnetic fields or contact currents is needed. In these instances, the highly accurate and specialized methods for individual neurons can be exchanged for more general methods. For use in the development of the retinal prosthesis, an admittance method was selected for its simplicity, efficiency, and flexibility.

1.5 Admittance Method

The Admittance Method was introduced by Armitage et al. in 1983 to calculate the power dissipation in body tissue due to RF induced hyperthermia. [9] It is a simple method that can be used to calculate the current distribution generated in complex, arbitrarily shaped biological bodies. The method maintains its basic simplicity regardless of the complexity of the subject under consideration, making it particularly useful for the geometries encountered in anatomically accurate biological models.

The method first requires a discrete model representing the object under consideration to be generated. In addition to spatial information, this model must also include the dielectric properties (σ and ε) of all materials. Then using this spatial and dielectric information in the model, an impedance (or admittance) network is built that electrically

approximates the object of interest. This resulting network is a grid of electrical nodes interconnected by impedances; in essence, it is a large linear circuit. Then the current stimulus is injected into the desired node(s) and the circuit can be solved.

The Impedance Method is a simulation scheme similar to the Admittance Method introduced by Gandhi in 1984. [10] It was introduced to calculate the electrical activity in arbitrarily shaped biological bodies exposed to quasi-static magnetic sources. The primary distinction between the impedance and admittance methods is that the impedance method solves mesh current equations while the admittance method solves node equations, meaning that a vector of unknown currents is found rather than unknown voltages.

While the simplicity of these methods allows the simulation of complicated geometries, they are limited by the availability of computational resources. Eberdt [13] implemented a multi-resolution meshing scheme for a two-dimensional impedance method which allowed the simulation of large, high resolution models with high voxel counts in an efficient manner. He showed that the size of the impedance mesh could be significantly reduced while sacrificing approximate 4.5% accuracy in current density calculations. The objective of these space reducing algorithms was to reduce the number of unknown variables in the linear system so that simulations could be run that would otherwise be prohibited by computational limitations.

Chapter 2

Basic Admittance and Impedance Methods

The Admittance Method is a scheme introduced by Armitage et al. in 1983 for the simulation of quasi-static electromagnetic radiation problems. [9] In 1984, Gandhi introduced the dual of the Amittance Method, the Impedance Method. [10] These are conceptually simple techniques that allow the simulation of complicated heterogeneous materials exposed to arbitrarily complex, spatially varying electromagnetic stimuli. These methods represent the physical object to be simulated as a network of impedances that corresponds to the electrical properties of the object. Then, an electromagnetic stimulus is applied and the response calculated by solving a linear system. Specifically, the Impedance Method solves the system $\mathbf{Z}\underline{I} = \underline{V}$ over a coordinate space while the Admittance Method solves a system $\mathbf{Y}\underline{V} = \underline{I}$. Which method is used depends on the type of stimulus that will be applied. The Impedance Method generates a set of loop equations, while the Admittance Method generates node equations. In the admittance method the total current

through the node must sum to zero. Because admittance methods use a current summing principle, current sources and sinks at nodes can be introduced. This makes the Admittance Method applicable to the desired application of simulating current densities resulting from injected contact currents. Therefore, the Admittance Method was used for our simulations.

Like most computational methods, the admittance method uses discrete calculations to approximate continuous phenomena. This requires a discrete model of the actual physical body of interest. The discrete model consists of cells arranged in a regular manner. For three-dimensional admittance method calculations, these cells are simply cubes arranged in a Cartesian coordinate system. An impedance model is derived for each cell based on the dielectric properties of the material the cell represents. Finally, the impedance models of all cells are connected into a large network which approximates the electrical properties of the object.

The Admittance Method used here can be viewed as having five distinct steps: discretization of the physical model, generation of the admittance network, calculation of node voltages, calculation of the branch currents from the node voltage differentials, and calculation of current densities from branch currents. Because discretization of physical models is not integral to understanding the theory behind the method, it will not be included.

For the remainder of this thesis, the terms Impedance Method and Admittance Method will be used interchangeably. Since the methods are conceptually identical, this ambiguity should not cause confusion.

2.1 Construction of the Impedance Network

For a cubic cell representing a material with generic conductivity, $\underline{\sigma} = [\sigma_x, \sigma_y, \sigma_z]$, generic permitivity $\underline{\varepsilon} = [\varepsilon_x, \varepsilon_y, \varepsilon_z]$ and dimensions *x'*, *y'* and *z'*, the value of the x-directed impedance of the material would be given by

$$Z_x = \frac{l_x}{A_x}\frac{1}{\sigma_x + j\omega\varepsilon_x} = \frac{x'}{y'z'}\frac{1}{\sigma_x + j\omega\varepsilon_x} \tag{2.1.1}$$

Similarly, (2.1.1) could be applied to the y and z impedance components by interchanging *x'*, *y'*, *z'*, and the dielectric values appropriately. It should be noted that anisotropic materials can be compactly defined because the dielectric values $\underline{\sigma}$ and $\underline{\varepsilon}$ are vectors and can vary directionally. Therefore, if the anisotropy can be represented in a consistent manner along the orthogonal x, y, and z axes, these types of materials can be represented without adding complexity to the method.

Using (2.1.1), an impedance model for a cube of material can be built such that each directional component of the cube's impedance is included. A simple cell splitting scheme is used in which the face of each cell is divided into quadrants where each of these quadrants will be the area used to calculate an impedance. Figure 2.1 demonstrates these divisions for the x-directed impedances. When the same is done with the y and z components, the impedances are combined into a unified model as shown in Figure 2.2.

After impedance models for each cell are generated, they are then placed together in a final mesh. The models are connected at the nodes, which are located at the corners of each cell. This results in parallel impedances which can be combined as shown in Figure 2.3. Therefore, impedances from adjacent cells that share a common edge will

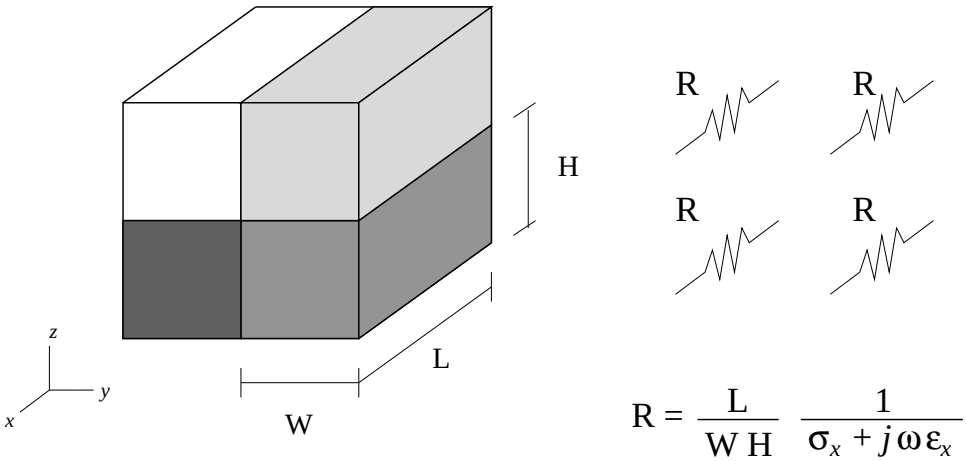

Figure 2.1: Derivation of x directed impedances for a single cell.

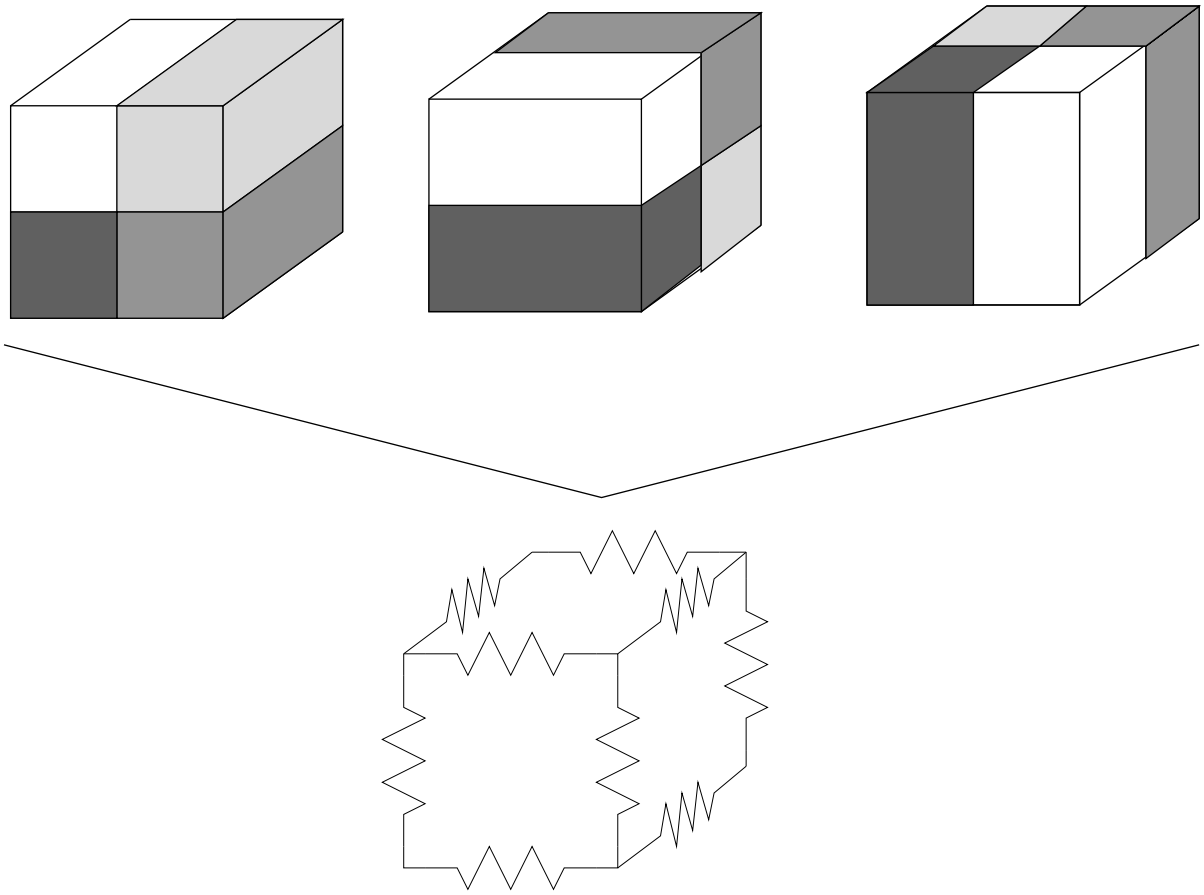

Figure 2.2: Divisions of impedances for all directional components and final impedance model for a single cell.

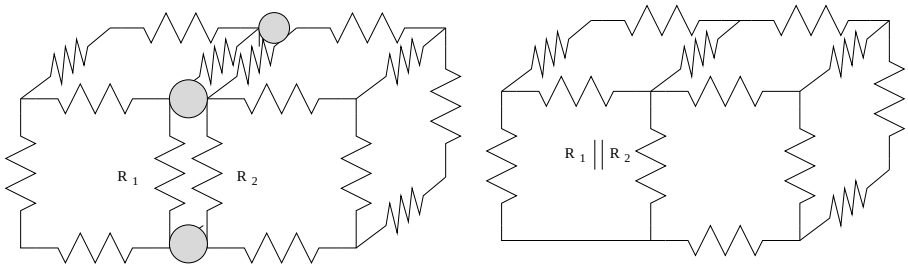

Figure 2.3: Two adjacent cells, the visible shared nodes are indicated by gray ovals (left). An equivalent model after combination of nodes and parallel combination of resistances R1 and R2 (right).

be represented by a single impedance in the final network.

The result of the impedance generating scheme is a three-dimensional lattice of impedances which can emulate the low-frequency electrical properties of any medium with known dielectric properties. Two special cases, however, are the inclusion of perfect conductors ($\sigma = \infty$) and perfect insulators ($\sigma = 0$). Perfect insulators would be theoretically represented by infinite impedance. Since no current would flow through infinite impedance, these can be omitted from the final network. Perfect conductors, however, are not handled as simply. Because the method is based on Ohm's Law, determining the current through an impedance of zero requires a division by zero, meaning current distribution within a conductor cannot be determined. However, the method can still be applied if the nodes connected by zero impedance are treated as one super-node as shown in Figure 2.4. This does not introduce error when applied under the quasi-static assumption, meaning that all nodes connected by a zero impedance would have the same voltage, and current continuity is still satisfied. So, while current densities within the conductor are not determined, the simulation can still proceed.

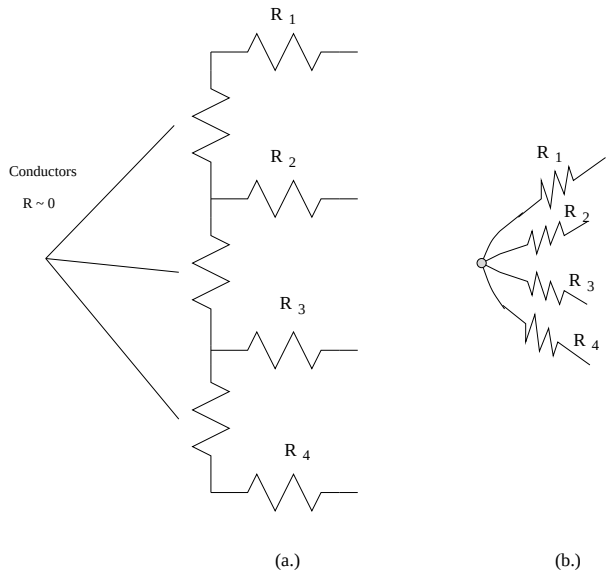

Figure 2.4: Two adjacent cells, the visible shared nodes are indicated by gray ovals (left). An equivalent model after combination of nodes and parallel combination of resistances R1 and R2 (right).

2.2 Application of Electromagnetic Stimuli

After the admittance matrix is constructed, four types of stimuli can be applied: incident magnetic field, incident electric field, and direct voltage and current stimuli. The presented Admittance Method uses current source stimulation to approximate the application of contact currents in the retina. However, other methods will also be introduced.

2.2.1 Magnetic Field Stimulation

Effects of magnetic field stimulation are calculated from Faraday's Inductance Law:

$$\oint_L \mathbf{E} \cdot d\mathbf{l} = -j\omega \int_S \mathbf{B} \cdot d\mathbf{S} \tag{2.2.1}$$

This condition is applied in discrete form to each cell in the mesh. Each cell face serves as the area **S** through which the B field integration is performed. Each cell face

then defines a loop in which an eddy current will result. If the B-field is applied over an entire face of an object, a set of mesh equations results. These mesh equations can then be solved and the net branch currents found.

Magnetic field stimulation is particularly well illustrated by the two dimensional case. Using Figure 2.5, the mesh equation for the central cell would be

$$V_1 + V_2 + V_3 + V_4 = -j\omega \int_S \mathbf{B} \cdot d\mathbf{S} \tag{2.2.2}$$

The only B field component that can be considered is normal to the two-dimensional plane; B-field components that lie in the two-dimensional plane would generate mesh currents normal to the plane, and thus cannot be included in a two-dimensional simulation scheme. In the three-dimensional case, however, B-field components can have arbitrary orientations if they are defined as vector combinations of components oriented along the Cartesian axes.

2.2.2 Incident Electric Field Stimulation

Electric field stimulation is more difficult to use than magnetic stimulation because there is no law that can be directly applied in a similar manner as the inductance law. However, we can use the conductivity of the medium in which the object is placed to distinguish between two separate cases that can be approached in different ways. One case is specialized for insulating media and the other for conductive media.

If the conductive object is placed in an insulating medium then electric field stimulation requires application of the following electric field boundary condition: that the

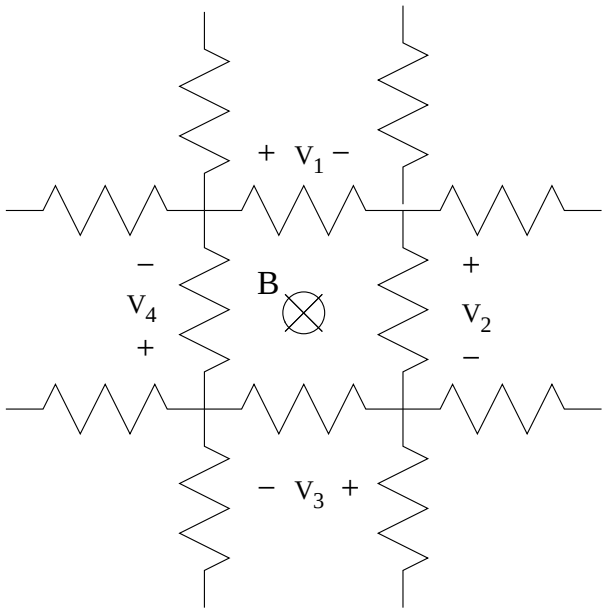

Figure 2.5: Visualization of 2.2.2.

electric flux density normal to a boundary must be equivalent across that boundary in the absence of free surface charge. This means that the normal component of the current cannot change abruptly across the boundary. Assuming a boundary between a non-conductive medium (air) and the conductive object to be simulated, the mathematical statement of the boundary condition is:

$$j\omega\varepsilon_{insul}\int_S \mathbf{E}_{insul}\cdot d\mathbf{S} = (\sigma + j\omega\varepsilon_{cond})\int_S \mathbf{E}_{cond}\cdot d\mathbf{S} \tag{2.2.3}$$

There are multiple approaches to applying this equation to an impedance network. One method, proposed by Eberdt, assumes that the object is small and highly conductive. This allows us to assume that the surface of the entire object is approximately equipotential, and that the incident electric field will be normal to the object surface. Then, (2.2.3) is applied to determine current density induced in the object. Finally,

impedances that lie along the conductor-insulator interface are removed. (This is acceptable because the surface is assumed to be equipotential, meaning that no current would flow through these impedances.) Then, ideal current sources are connected along the edges of the object to induce the currents calculated from (2.2.3). Finally, the current sources are connected together to complete the circuit.

The above scheme assumes that the object is surrounded by an insulating medium, but in many cases that arise in biomedical applications, the medium is a body fluid that has significant conductive properties. In the low frequency case, the current density will be directly proportional to the E-field via the relation $J = \sigma E$. With this formulation, the E-field can be simulated indirectly by orienting current sources in the proper direction. The next section introduces these current sources.

2.2.3 Direct Injection of Currents and Voltages

Current source stimulation is used in the work presented in later sections of this thesis. Injection of currents is the most flexible and most easily applied method of stimulation for the Admittance Method. Because the admittance mesh is effectively a large linear circuit, conventional techniques for solving linear circuits can be applied. Furthermore, the method can be used to generate SPICE compatible codes so that SPICE engines can be used to solve the mesh. Unfortunately, due to the large amount of memory necessary to run large simulations with SPICE, it was not applicable for our admittance method. Instead a custom solver was written using the IML++ templates based on Krylov-space iterative methods [14].

2.3 Construction of Linear System for Direct Current Injection

In our method, it was needed to simulate the injection of currents from contact electrodes. With this in mind, construction of the admittance matrix follows in a straightforward manner from conservation of current at each node in the impedance model. A typical node is shown in Figure 2.6 with the surrounding nodes and connecting impedances. The following expression is found by equating the input and output currents at node n_0.

$$I_1 + I_2 + I_6 = I_3 + I_4 + I_5 \tag{2.3.1}$$

$$\frac{V_1 - V_0}{Z_1} + \frac{V_2 - V_0}{Z_2} + \frac{V_6 - V_0}{Z_6} = \frac{V_0 - V_3}{Z_3} + \frac{V_0 - V_4}{Z_4} + \frac{V_0 - V_5}{Z_5} \tag{2.3.2}$$

If (2.3.2) is rearranged and factored for the node voltages then we get

$$\frac{V_1}{Z_1} + \frac{V_2}{Z_2} + \frac{V_3}{Z_3} + \frac{V_4}{Z_4} + \frac{V_5}{Z_5} + \frac{V_6}{Z_6} - V_0 \left[\frac{1}{Z_1} + \frac{1}{Z_2} + \frac{1}{Z_3} + \frac{1}{Z_4} + \frac{1}{Z_5} + \frac{1}{Z_6} \right] = 0 \tag{2.3.3}$$

An expression of the form of (2.3.3) is written at every node in the impedance network. The zero on the right side indicates that all currents into and out of node n_0 (with voltage V_0) are accounted for by the connections with adjacent nodes.

Current sources introduced into the mesh force a predetermined current between nodes. For the practical purposes of solving the linear system, a single node must be arbitrarily designated as having a potential of zero. (This is the same requirement found

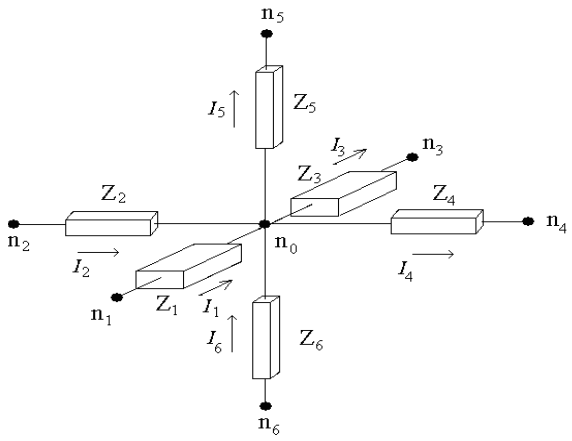

Figure 2.6: Orientation of nodes, impedances, and currents for constructing node equation.

in SPICE simulators.) For our purposes of simulating various electrode shapes, all current injection points are electrodes that are approximated as perfect electric conductors. When the impedance network is generated, each electrode would be collapsed into single super-node as shown in Figure 2.4. Current sources are then implemented by forcing current into one electrode super-node and extracting it from another as shown in Figure 2.7. At these current insertion points, the form of (2.3.3) is modified by adding the current amount to source or sink from the electrode to the right side of the equation. The sign of this current differentiates between a sink point or source point. For the system in Figure 2.7, the equation at the super-node representing electrode A would be written as:

$$\frac{V_1}{Z_1} + \frac{V_2}{Z_2} + \frac{V_3}{Z_3} + \frac{V_4}{Z_4} + \frac{V_5}{Z_5} + \frac{V_6}{Z_6} - V_0 \left[\frac{1}{Z_1} + \frac{1}{Z_2} + \frac{1}{Z_3} + \frac{1}{Z_4} + \frac{1}{Z_5} + \frac{1}{Z_6} \right] = -I_a \quad (2.3.4)$$

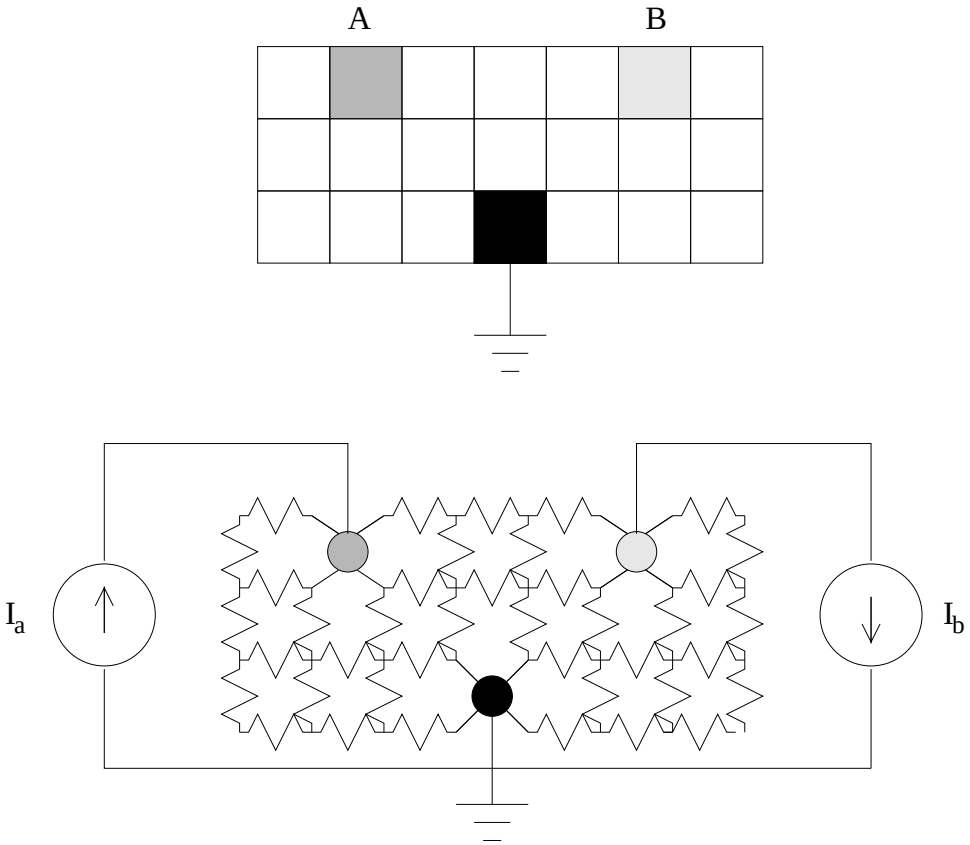

Figure 2.7: Visualization of method by which currents are introduced into the impedance network through electrode super-nodes. The darkened cells in upper diagram represent perfect conductors used as current injection points. Circles in lower diagram indicate super-nodes.

2.4 Derivation of Branch Currents and Current Densities

After the linear system is solved for the node voltages, the resulting branch currents in the mesh are calculated. Because each impedance in the final network represents a parallel combination of impedances, it is necessary to divide the current appropriately. The proper currents can be found without explicit current division by applying Ohm's law directly using the node voltages and the contributing impedance values for each cell. Referring to Figure 2.8, I_a would be found by:

$$I_a = \frac{V_1 - V_0}{Za} \tag{2.4.1}$$

After the currents are found, each cell has a total of 12 current values, 4 directed along each axis. This directionality will be maintained in the current density calculations, meaning the result will be a vector quantity. In a cell, the four currents in a given direction are first converted to current densities by dividing each current by its corresponding area. Referring to the dimensions shown in Figure 2.8, the x-directed current density resulting from the current I_a is given by:

$$J_x = \frac{I_a}{\left(\frac{\Delta y}{2}\right)\left(\frac{\Delta z}{2}\right)} \tag{2.4.2}$$

Subsequently, identical calculations are performed for the remaining three quadrants of the cell. The four resulting values are then averaged to find the x-directed current density at the cell centroid. This operation is then performed for the y and z components to obtain the complete vector current density for the cell.

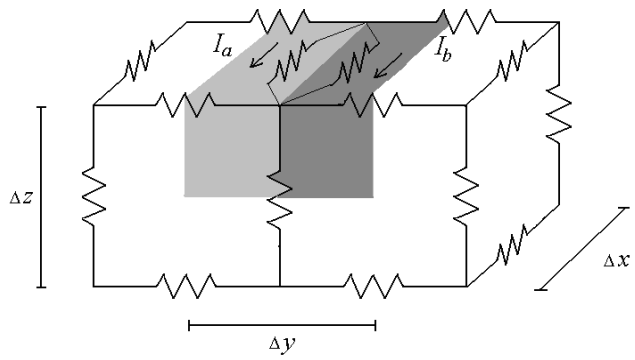

Figure 2.8: Visualization of method by which currents are introduced into the impedance network through electrode super-nodes. The darkened cells in upper diagram represent perfect conductors. Circles in lower diagram indicate super-nodes.

Chapter 3

Three-Dimensional Multi-Resolution Admittance Method

While numerical computational methods allow the solution of electromagnetic problems that would be otherwise unsolvable, the availability of computational resources places limits on the complexity and maximum spatial size of the problem. In the admittance method, the memory and processing time required to solve a large linear system limit the size of the simulation space. Furthermore, because the size of the linear system is directly related to the number of computational cells, three-dimensional simulations become large as resolution is increased. Consider that a cubic model with 64 cells per side has a total of 262,144 cells, but a model of 128 cells per side is eight times the size at 2,097,152 cells. Therefore, doubling the fundamental dimensions of the simulation space (or equivalently increasing the resolution by a factor of two) requires an eight-fold increase in computational resources.

To this point, storage of the model in memory has been neglected from the discussion.

In a uniform resolution method, the model can be stored as a three dimensional array, using a simple indexing scheme to indicate location. This scheme is efficient in terms of memory because each cell can be stored using only a single byte, allowing large models to be accommodated. However, while large models can be stored, in the admittance method, each cell comes with a computational cost in the form of enlarging the linear system. In order to simulate large, high-resolution models, either the computational cost per unit cell must be reduced or else the total number of computational cells must be reduced while preserving the spatial information of the model. Due to the realities of solving a linear system, the former is not possible. The latter, however, can be achieved by applying a multi-resolution gridding scheme.

In admittance method simulations, memory consumption primarily occurs in two stages: 1.) storage of the model in physical memory, and 2.) solution of the linear system. By applying a multi-resolution algorithm, the size of the linear system can be reduced at the expense of complicating the model storage scheme. In multi-resolution models, the regularity of the mesh is disrupted, and the location of each cell can no longer be identified by simple array indexing. Rather, each cell, formerly represented by a single byte, must now contain information indicating the location and volume of the space it occupies. Furthermore, a data structure must be created to organize the cells so they can efficiently communicate within the code. Due to the added complexity of the data structure, Eberdt found it unlikely that multi-resolution simulations will significantly reduce the memory consumption involved with building the impedance mesh. [13] However, reducing the number of cells in the model correspondingly reduces the size of the linear system, thereby reducing the amount of time required to find the solution. Consider that a simulation

of a cubic space with 256 cells per side generates a linear system with over 16 million unknowns; the time required to solve the system is considerable even with today's fast processors. Therefore, a three-dimensional multi-resolution method was implemented. The remainder of this chapter will detail the basic methods employed for applying three-dimensional multi-resolution meshing to the admittance method.

3.1 Space Decomposition Considerations

The space decomposition scheme aims to reduce the number of computational units while preserving the spatial information contained in the model. However, we must consider the error introduced by the multi-resolution scheme. The basic approach is to use the maximum resolution (smallest cell size) close to material boundaries in the model, and gradually expand the cell size into homogenous space. The strategy assumes that in homogenous space, the current density will not change abruptly as there are no material disruptions. To ensure a gradual transition from small to larger cells in only homogenous space, the following rules are followed:

- All cells bordering any cell of a different material must be the maximum resolution (smallest cell size.)
- No cell may have a dimension greater than twice the size of the smallest dimension of any adjacent cell.
- All cells will be cubes, having equal dimensions along each axis.

3.2 Data Structures

The data structure has two functions in our multi-resolution meshing algorithm. First, it allows irregular multi-resolution data to be efficiently stored and accessed. Second, the nature the structure dictates the manner in which it is built, and hence the algorithms used to decompose space cannot be independent of the data structure. In computer graphics, octrees are a type of data structure used to store three-dimensional multi-resolution spaces. The octree breaks a heterogeneous cubic volume into eight equally sized octants, and each of these is further subdivided in a similar way, and the process continues recursively. The recursive division stops when each octant either 1.) contains cells of only one type or 2.) contains cells of the maximum possible resolution (the inherent resolution of the model.) In his two-dimensional code, Eberdt used a different type of data representation, a linked mesh structure. In linked mesh structures all cells possess pointers to all neighbors and adjacent cells are recursively combined into fewer larger cells. These two structures require opposite construction approaches: the linked list approach starts with the maximum possible number of cells and reduces this quantity, while the octree begins with a single cell representing the entire space and gradually subdivides cells where necessary. Both structures have strengths and weaknesses, and these will now be discussed briefly.

Figure 3.1 shows a multi-resolution space, and the corresponding linked-mesh in Figure 3.2 and quadtree in Figure 3.3. (For this explanation, two-dimensional structures are used because they can be easily represented graphically. Extension to three dimensions is straightforward.) Each cell in the linked mesh has pointers to all of the adjacent cells.

This allows each cell to communicate directly with all of its neighbors without being reliant on any intermediary. Conversely, the cells in the quadtree structure do not communicate directly with each other; rather they must communicate indirectly through an upper level node in the tree for information about their neighbors. This difference means that linked mesh structures are more flexible than quadtrees because there is only one level of data pointers. Virtually any possible configuration of cells can be represented in a linked mesh configuration. The quadtree representation, however, inherently places limits on which cells can be combined. For example, in Figure 3.4 cells A and B cannot not be combined unless the entire space was homogenous and represented by a single cell. The deviating material requires the area be decomposed into four separate cells, requiring the space in cells A and B be split, even though they consist of the same material.

While the linked-mesh structure is more flexible than the tree-based methods, the tree-methods are more memory efficient. In Figures 3.2 and 3.3 each connection represents two memory pointers. The quadtree requires 56 pointers while the linked mesh requires 76 pointers. This difference is typical in two dimensional simulations. However, in three-dimensional structures, the disparity becomes even greater as the number of cell neighbors increases. In the simplest possible three-dimensional case, in which the space consists of eight cells (2 x 2 x 2), an octree requires 16 data pointers and a linked-mesh requires 24.

As noted previously, the nature of each data structure dictates the manner in which it must be constructed. Differences in both time and memory required to build each type of structure favors the use of the octree which was ultimately chosen for this reason. Tree structures begin with a single node in the tree, and gradually build the tree, adding

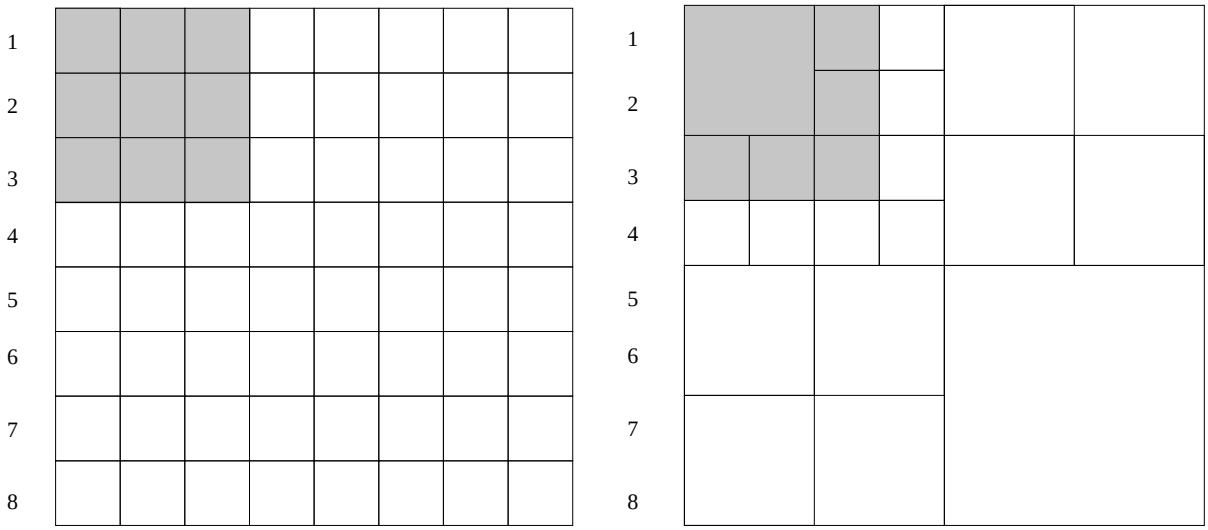

Figure 3.1: Unit resolution space and a possible multi-resolution breakdown of that space. Notice in the multi-resolution space that the three constraints are respected.

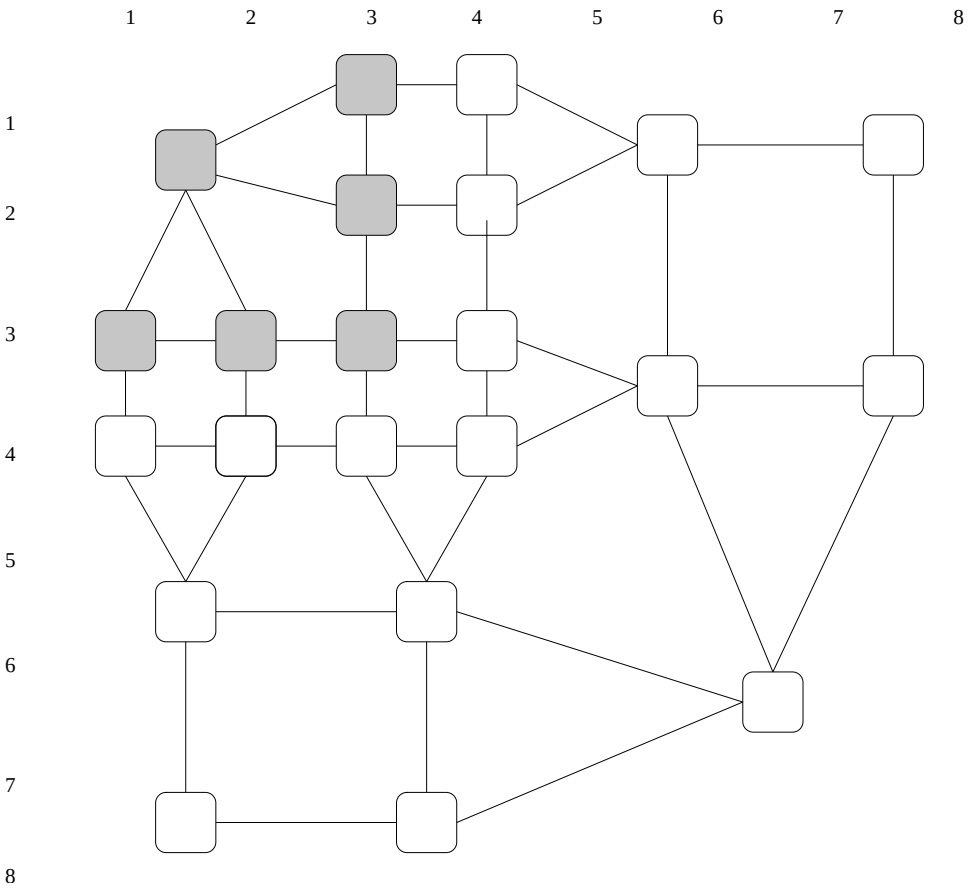

Figure 3.2: Linked-mesh representation of multi-resolution space in Figure 3.1

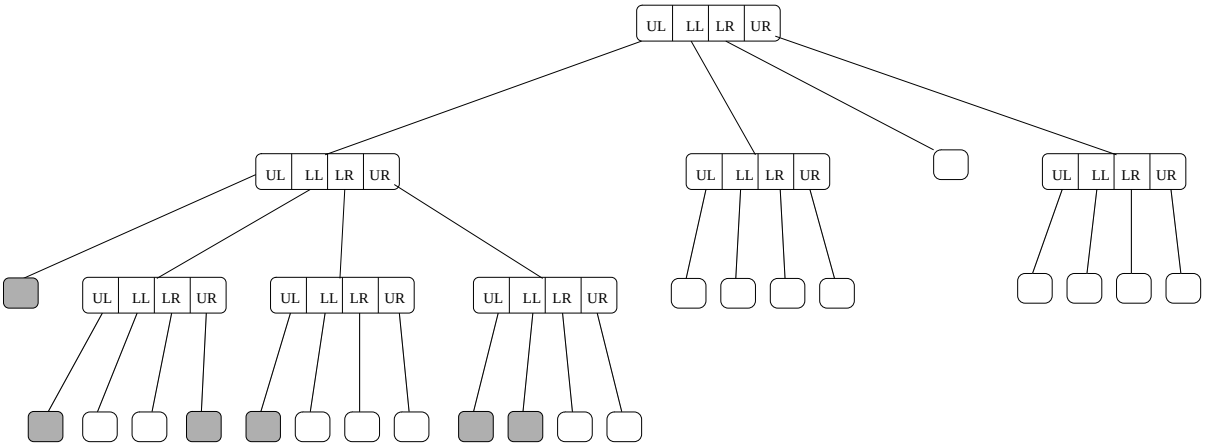

Figure 3.3: Quadtree representation of multi-resolution space shown in Figure 3.1. For the locations, the first letter indicate U = Upper, L = Lower. The second letter L = Left, R = Right.

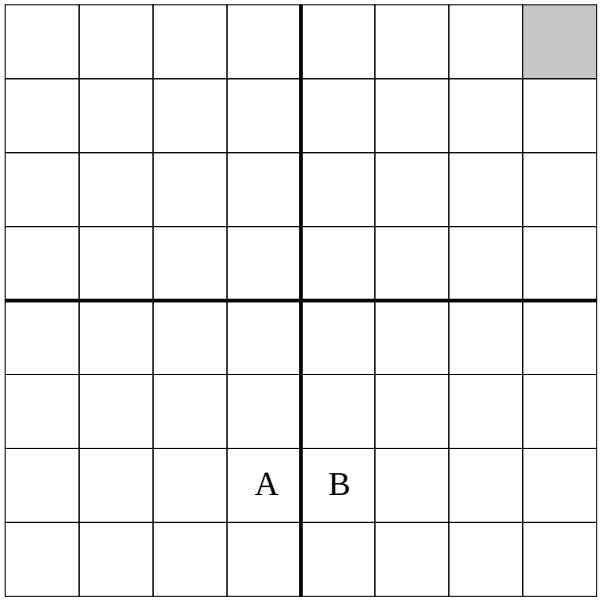

Figure 3.4: Cells A and B cannot be combined if a quadtree is used. The single grey cell requires that the divisions shown in bold are made, separating cells A and B.

additional branches as needed. This has the advantage that the maximum memory required during the building process is equal to the amount necessary to store the final tree; no additional memory is needed in the construction process. Linked-mesh structures, however, first require the entire model be constructed with unit-resolution cells, and then these are iteratively combined until no more combinations are possible. The principle disadvantage is that the maximum possible amount of memory that can be used to represent the structure is required, meaning that a computer capable of storing the final multi-resolution structure in memory may not be capable of building it.

Because the process of building a linked mesh requires an unknown number of iterations before optimum space decomposition is achieved, the processing time required is unpredictable, and can become quite large. Octree structures, however, reach a definitive end point, and since the size of the space to be decomposed places a limit on the number of recursive operations, processing time to build the system is predictable, and predictably shorter than linked mesh operations.

3.3 Mesh Construction

An octree scheme was implemented for the three-dimensional admittance method code due to its efficient use of memory and quick build time. A major limitation of the octree is that it requires the simulation space have equal dimensions along all three axes and that this dimension be a 2^n where n is an integer. This limitation was accepted at the outset, and does limit the sizes of model space that can be simulated. However, modifications could be made which would allow the tree to accommodate models of

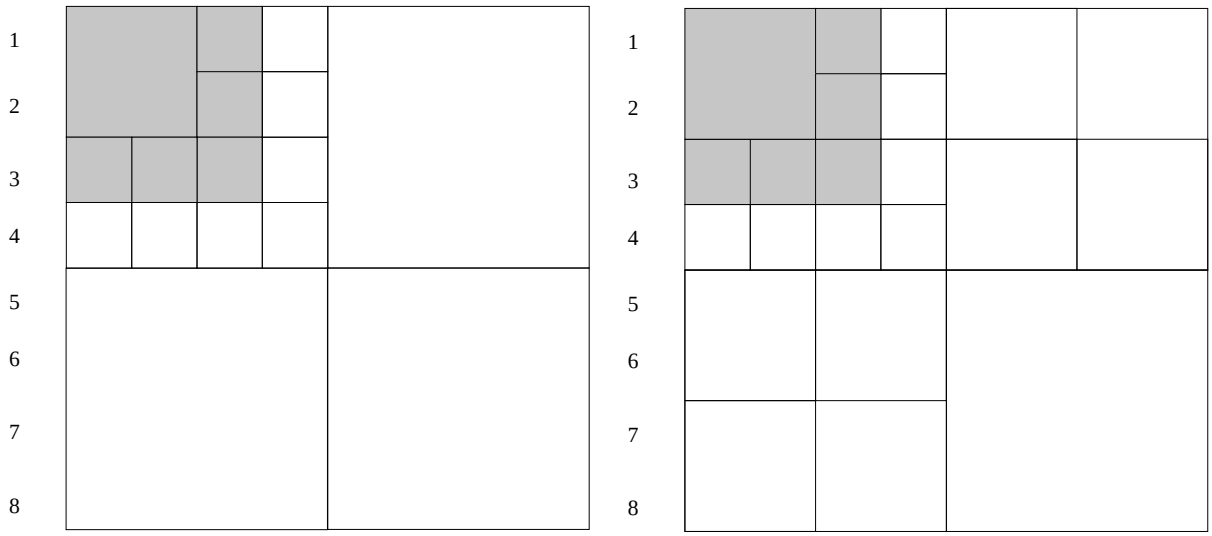

Figure 3.5: Comparison between tranditional quadtree space decomposition (left) and that modified to respect 2:1 ratio requirement (right).

arbitrary dimensions, but due to the added complexity, this was not implemented.

Octree construction begins by dividing the cubic space into eight equally sized octants by dividing the space in half along each dimension. Then each octant is evaluated to determine if further division is necessary. It is in this determination that our implementation of the octree deviates from a standard implementation. In regular octrees, each octant is only subdivided if the cells located within each octant are of differing types, for our purposes, however, we must remember the constraints that require unit resolution cells along material boundaries and that each cell may only have a dimension twice the size of any adjacent cell. Figure 3.5 shows the standard quadtree decomposition of the space in Figure 3.1 and a quadtree of the same space modified to respect our conditions for cell size. The challenge now becomes determining criteria that will allow building the octree in a way that will respect our conditions.

Figure 3.6 shows the gradual expansion of cells away from a material boundary and

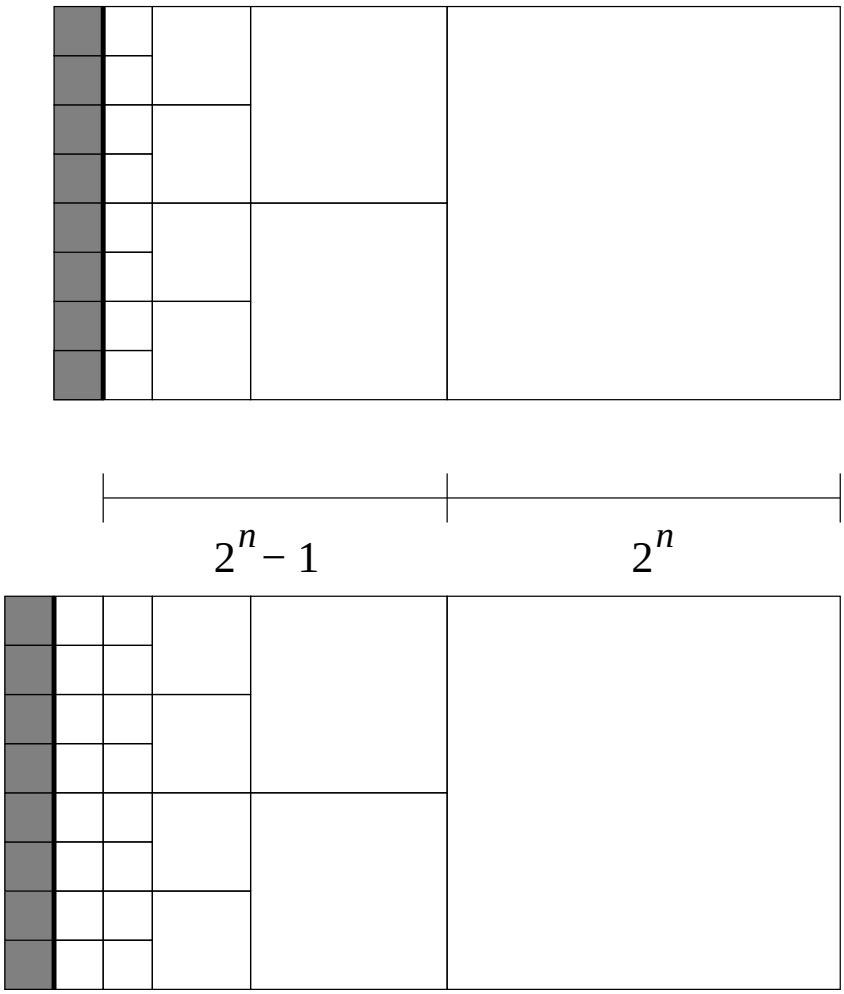

Figure 3.6: Expansion of multi-resolution cells away from material boundary. For a cell to have dimension 2^n, the region within $2^n - 1$ of that cell's boundary must be homogenous. In some cases, the region 2^n will be the actual condition due to the nature of the tree.

into homogenous material. Since we know that 1.) each cell in an octant must be the same size and 2.) each cell can only have dimensions twice the size of an adjacent cell, we use Figure 3.6 to form the following conjecture: A cell with fundamental dimension 2^n will not violate size constraints if all cells within a distance of $2^n - 1$ from any edge or face of the cell consist of the same material type.

3.4 Derivation of Multi-Resolution Lumped Impedances

The multi-resolution meshing scheme introduces new geometrical orientations of cells. In a unit resolution admittance method, the dimensions used to calculate the impedances for each cell region are the same for each impedance. In a multi-resolution scheme, however, the dimensions become irregular. Furthermore, because two cells of equivalent size can have varying numbers of neighboring cells, the impedance model used for these equivalent cells must be different. The development of these models is now discussed.

The impedance model of each cell type must meet two requirements; it must 1.) accurately model the internal electrical properties of the cell and 2.) interface properly with the impedance models of adjacent cells. The first of these requirements is purely a function of the size and shape of each individual cell. The second condition, however, requires consideration of a cell's external neighbors. In the unit resolution method previously described, the second condition was met by connecting the impedances at the corners of each cell because when the cells were juxtaposed in the final mesh, the corners naturally made contact. In multi-resolution schemes, the same basic approach will be maintained in that every cell corner will become the location of a node, and impedances will still spatially relate to the edges of each cell. However, because two or more cells can meet along the edge of a larger cell as shown in Figure 3.7 a node must be placed in the middle of that edge. Also, because the edges of the smaller cells lie along the face of the larger cell, an impedance must also be placed there. In order to accommodate these changes, new impedance models for each cell were developed for all possible configurations.

Due to the 2:1 condition limiting variation in adjacent cell sizes, a multi-resolution

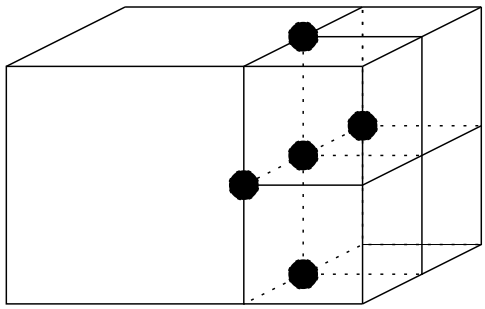

Figure 3.7: A 2x2 cube bordered on a side by four unit cells. The bold dots indicate the location of nodes that would not exist if the 2x2 cell was bordered by a cell of equal dimension.

cell with dimensions 2 x 2 x 2 that is completely surrounded by unit resolution cells has the maximum possible number of neighbors. This cell would have the corresponding impedance model shown in Figure 3.8. Other configurations of cell neighbors would require different impedance models, the systematic derivation of these models is as follows:

1. Nodes are placed at all corners of all cubes.

2. The edges of all cells are traced between nodes. Impedances will lie along these edges.

3. The area of each cell face is divided by tracing lines that are equidistant from the nearest two impedances that lie normal to the cell face. Using this methodology, the portion of each cell in closest proximity to each lumped impedance is determined. Figure 3.9 demonstrates all possible configurations that can be generated by this step.

4. The lumped impedances are calculated using the divisions determined in step 3.

By applying the above methodology to determine the directional impedances of each cell, accurate impedance models that can be integrated into the greater impedance net-

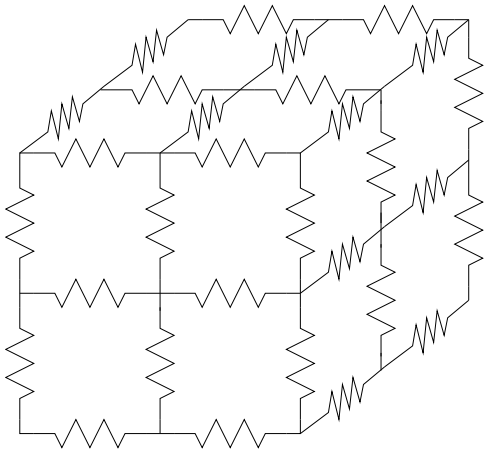

Figure 3.8: Impedance model of multi-resolution cell with maximum possible number of neighbors. Hidden sides are identical to visible sides.

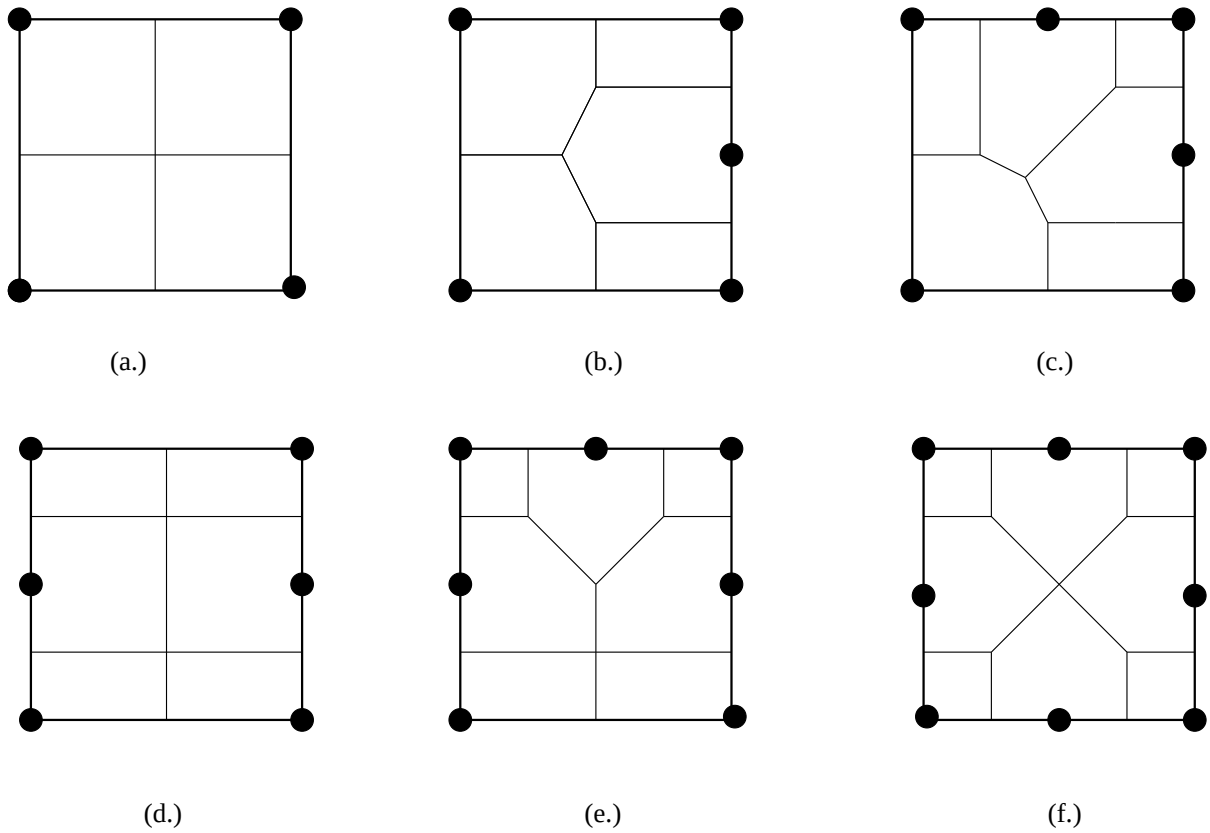

Figure 3.9: Possible orientations of resistors normal to the visible face of multi-resolution cell. Resistors will be located at the bold dots.

work are generated. It should be noted that the cross-sections of each cell will generally differ among the three axes and that the process must be performed twice for each axis because the two halves of the cell can have different configurations of cell neighbors.

3.5 Calculation of Current Densities

Because impedance models vary for each cell, the current density calculations must also vary accordingly. The impedance method calculates average total current densities within each cell. This means that our calculated value does not correspond to a specific point within the cell. In his two-dimensional method, Eberdt implemented an interpolation scheme that could estimate current densities throughout each cell and at junctions between cells. While this was useful for a two-dimensional method, in a three-dimensional code this type of calculation was impractical due to complexity. Furthermore, for our purposes of generating current intensity images of biological data, average values are more appropriate. So, our method reports three average directional current density values for each cell: J_x, J_y, and J_z.

Each average directional current density for the entire cell are found by determining the current density in each half of the cell and then averaging these values. Within each half-cell, current densities are calculated for each region of each cell face by dividing the branch current by the area of the cell faced used for deriving the corresponding lumped impedance. A weighted average of the directional current densities for each half-cell are then calculated, weighting proportionally to the area of each region. Then the average current density is the mean of these values for the front and back half of each cell. This

process is then performed to find the current densities in the remaining two directions.

Chapter 4

Three-Dimensional Simulation Results

Before the multi-resolution code was used for simulation of retinal prosthesis cases, extensive test cases were run to verify the proper functioning of the simulator. One of these is presented to demonstrate the operation of the simulator. A simple geometry is used that has an analytical solution. The computational results are then compared to the analytical result to show the accuracy of the method. Then the simulator is used to compare two possible retinal prosthesis electrode configurations and analyze their respective characteristics.

4.1 Spherical Demonstration Case

For a demonstration case, a simple geometry that can be solved analytically but is still sufficiently complicated to adequately demonstrate the capabilities of the simulator

is presented. To meet these criteria, a pair of concentric spherical electrodes was chosen. The inner electrode serves as the current source and the outer electrode as the current sink. The material between the two conductors is a homogenous conductive medium with conductivity $\sigma = 1$. A current is then injected from the inner conductor and extracted at the outer conductor. Figure 4.1 shows the basic geometry and values used for the simulation.

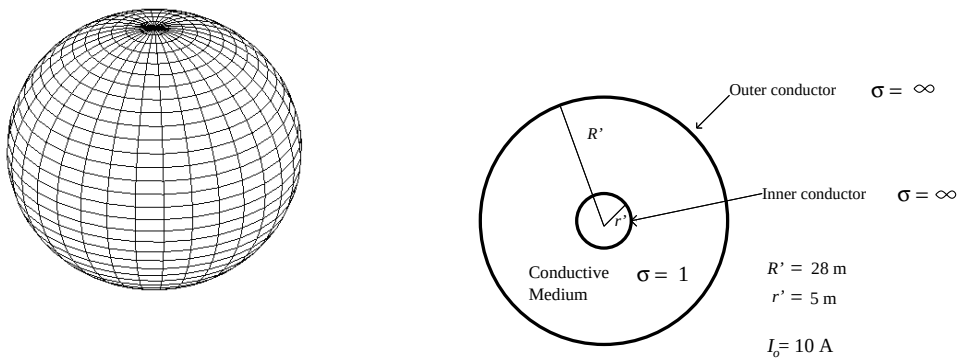

(a) (b)

Figure 4.1: Geometry used for test case, concentric spherical conductors serve as the source and sink electrodes.

The analytical solution for this geometry is found as a function of the radial coordinate. Due to perfect symmetry, current will spread uniformly in all radial directions between the two electrodes, with the highest current density around the inner, smaller conductor and gradually tapering off and reaching a minimum at the outer conductor. The theoretical current density as a function of the radial coordinate is found by dividing the total injected current by the surface area of a sphere with a radius defined by the radial coordinate:

$$J_r = \frac{I_o}{4\pi r^2} \tag{4.1.1}$$

Figure 4.3 shows a color intensity plot of the current densities found in a cross-section of the concentric spheres. As expected, the highest current density occurs around the central conductor and then gradually diminishes to a minimum at the outer conductor. Figure 4.4 shows a plot of calculated current densities between the two conductors. The discrete points show the current density calculated at the cell centroids, and the continuous line is the ideal current density line calculated from (4.1.1). From Figure 4.3 we can see qualitatively that the calculated values are close to the ideal values. Actual rms current density error was calculated by first finding the percentage error at each data point using (4.1.2). Then rms error was calculated by applying (4.1.3). (Note that the angle brackets indicate the mean of the set of J_{err}^2.) The final rms error was calculated to be 8.3945%.

$$J_{err_i} = 100 \left| \frac{|J_{ideal_i}| - |J_{computed_i}|}{J_{ideal_i}} \right| \tag{4.1.2}$$

$$J_{err_{rms}} = \sqrt{\langle J_{err}^2 \rangle} \tag{4.1.3}$$

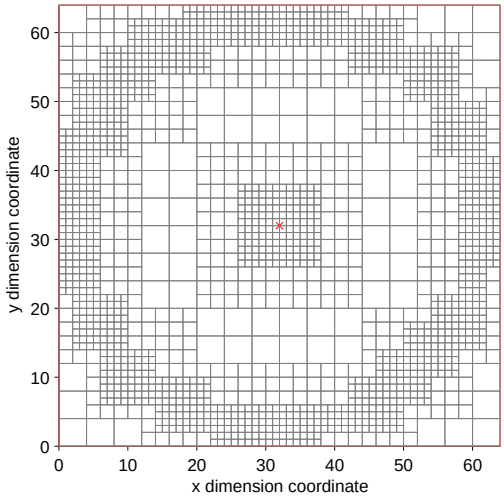

Figure 4.2: Cross section of multi-resolution of concentric spherical electrode test case. Total cell reduction was 58% (reduced to 109,068 multi-resolution cells from 262,144 unit cells.)

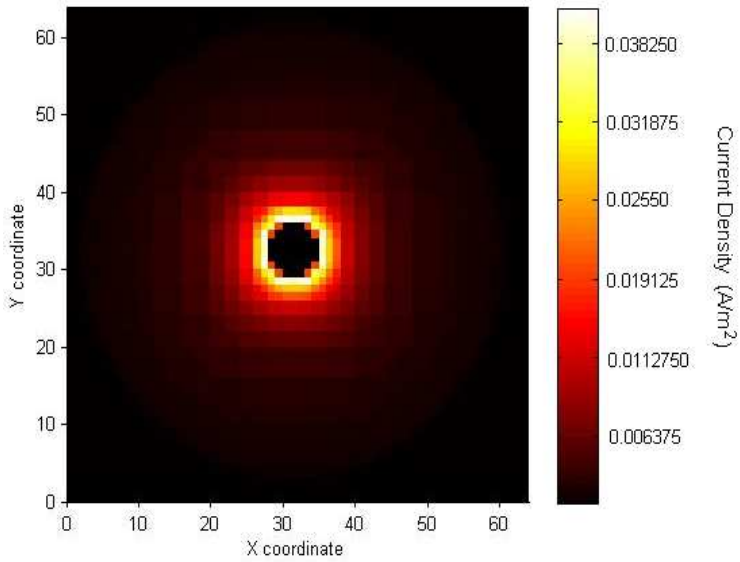

Figure 4.3: Cross section of multi-resolution of concentric spherical electrode test case.

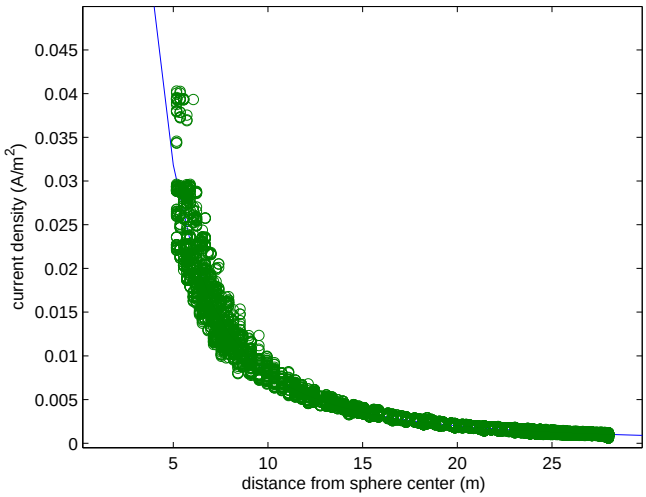

Figure 4.4: Plot of current densities calculated between inner and outer conductor. Total rms error was calculated to be 8.3945%

4.2 Two Configurations for Retinal Prosthesis Electrode Array

For a retinal prosthesis to function appropriately, the electrode array must be able to generate regions of high current density within the ganglion cell layer where neural stimulation is desired. However, these regions should be surrounded by areas of substantially lower current densities that are not stimulated. The sharper the drop off in current density, the more likely the current stimulus will be perceived as a discrete point of light in the visual field. If current were to spread significantly within the ganglion cell then the stimulus may instead be perceived as a large smear or streak as improper ganglion cells are stimulated.

One basic electrode design decision is on what surface the electrode array should be placed. The two basic electrode configurations illustrated in Figure 4.5 were considered.

The first, which was ultimately concluded to be the preferred solution, was an epi-retinal electrode array system. In this configuration the grid of stimulating electrodes is placed directly on the retina surface, and the current return (ground) is placed in the vitreous humor of the eye. The second option investigated was a trans-retinal configuration in which the grid of firing electrodes was located on the outside of the eye, placed directly against the sclera, and the current return was located inside the eye, against the epi-retinal surface. Both configurations have potential benefits and drawbacks which are beyond the scope of this thesis. The objective here is to report on their relative capabilities to steer current within the ganglion cell layer. The epi-retinal electrode configuration has the distinct advantage of placing the stimulating electrode array in very close proximity to the ganglion cell bodies that we wish to stimulate. From a current steering perspective, this is intuitively the more natural of the two configurations. However, it was necessary to compare the two configurations, to determine if both were potentially viable solutions worthy of further later investigation.

4.2.1 Modeling the Eye and Electrodes

Anatomically realistic models were developed to test epi-retinal and trans-retinal electrode configurations. The final model used was a hybrid of several different models. It was ultimately based on the Visible Human Project [19] in which an entire human male cadaver was used to create a discrete human model at a resolution of 1 mm. This model was interpolated to 0.25 mm resolution, and the eye of this model was replaced with an anatomically more detailed eye created by DeMarco [17]. Then, this hybrid model was

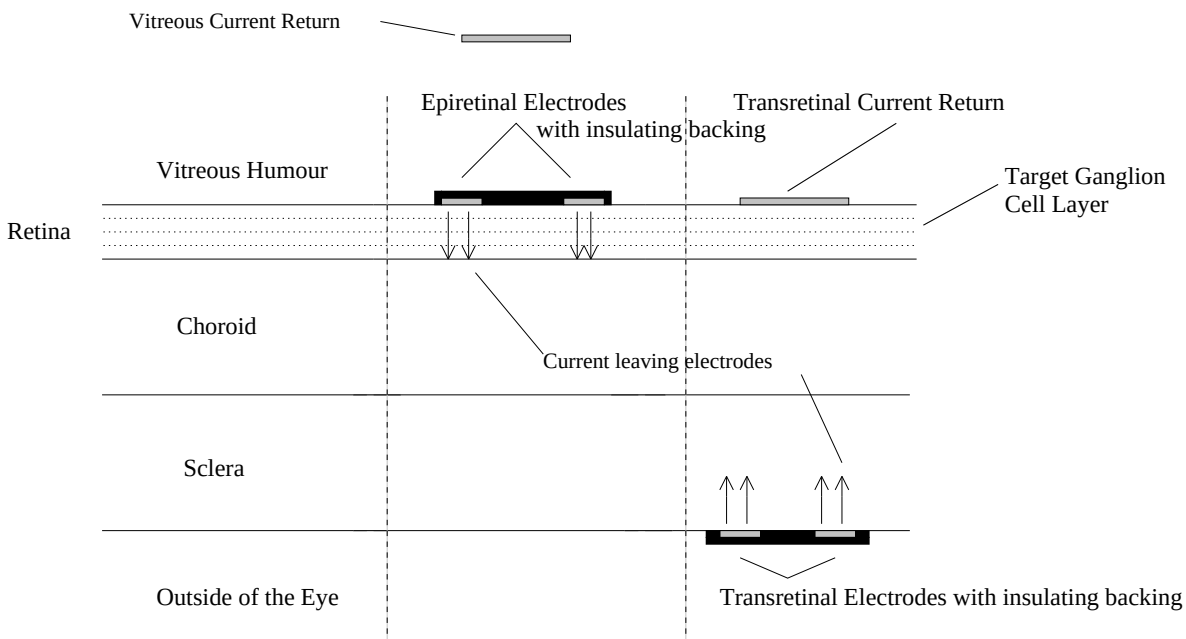

Figure 4.5: Geometry encountered in the tissues of the back of the eye and the locations of epi-retinal and trans-retinal electrodes.

further interpolated to 31.2 μm resolution and a stratified retina suitable for our uses was created and placed within DeMarco's model eye. (His original model defined the retina as a single tissue, rather than having distinct layers.) This retinal model was based on an SEM image of a stained retinal cross-section published by Rodieck [21]. The details of this retinal model are discussed in the next subsection.

The complete simulation space needed to represent the 8x8 array of electrodes, each approximately 100 μm in width and with equivalent separation. The need to meet this requirement and work within computational limitations restricted the simulation space to 128 cells per side. This necessitated the model be interpolated to a resolution of 31.2 μm.

Figure 4.6(a) shows a cross-section of the actual simulation space with the epi-retinal electrode placed within our model of the back of the eye. The electrode array for this

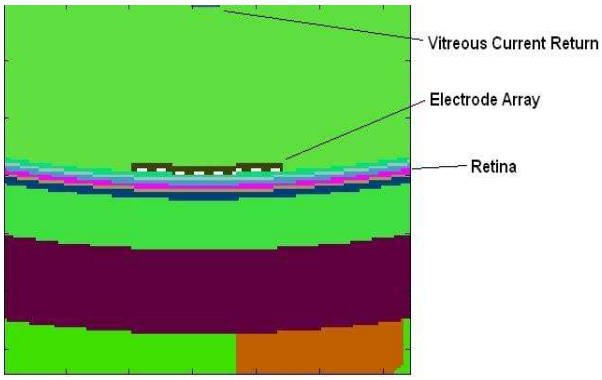

(a)

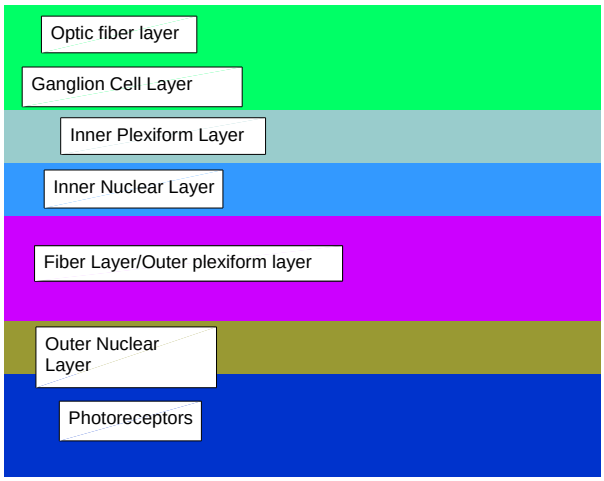

(b)

Figure 4.6: Cross-section in $x - y$ plane of simulation space for testing the epi-retinal electrode configuration (a). Closeup of retina model (b).

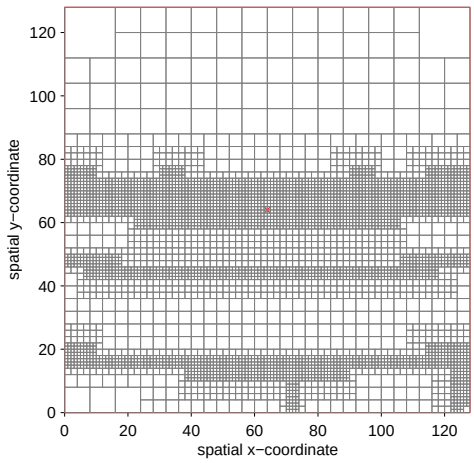

Figure 4.7: Multi-resolution mesh generated from model seen in Figure 4.6(a).

simulation was an eight by eight grid of square electrodes sized $127\mu m$ per side and each separated by $127\mu m$. Each electrode was used to injected a $600\mu A$ current, and the ground was placed in the vitreous, behind the electrode array. Table 4.1 lists the resistivity properties of the non-retinal tissues in the simulation space.

Table 4.1: Resistivity Values of Non-Retinal Tissues ($\rho = 1/\sigma$)

material	ρ (Ω·m)
choroid	1.080
sclera	1.98
vitreous humor	0.666
fat	50.000
generic muscle	4.130

The trans-retinal electrode configuration is shown in Figure 4.8(a). The same model of the posterior section of the eye used in the epi-retinal case is also used here. An identical electrode array was placed on the outside of the eye, behind the sclera, and the current return on the epi-retinal surface. As can be seen by comparing Figures 4.5, 4.6(a), and 4.8(a), it is unlikely that the trans-retinal configuration will have comparable performance

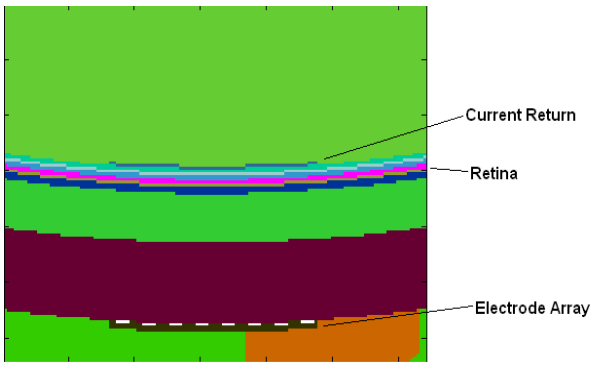

(a)

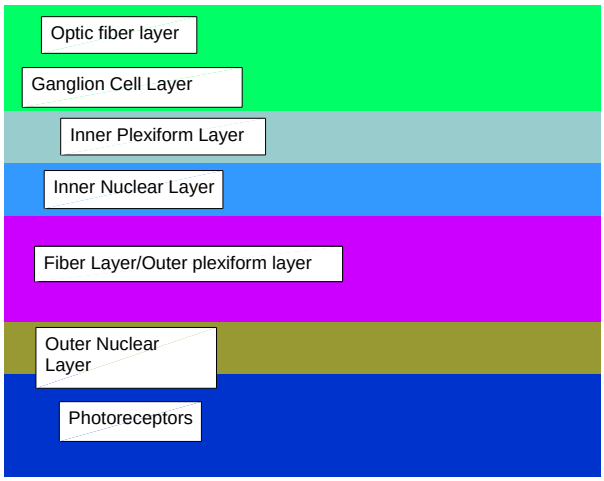

(b)

Figure 4.8: Cross-section in $x - y$ plane of simulation space for testing the trans-retinal electrode configuration (a). Closeup view of retina model

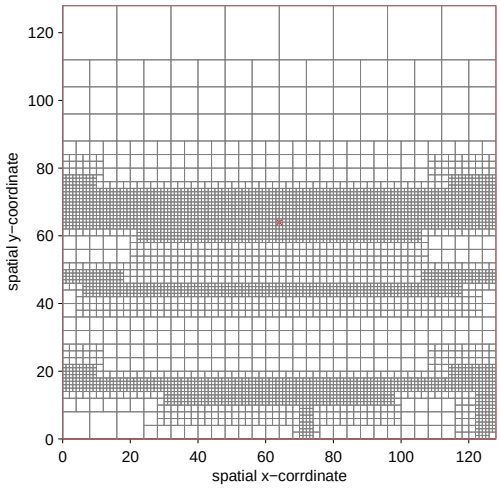

Figure 4.9: Multi-resolution mesh generated from model seen in Figure 4.8(a)

to the epi-retinal case because it places the electrodes much further from the target ganglion cell layer.

4.2.2 Stratified Retina Model

The retina model used for these three-dimensional simulations was the result of compromise. The need to accomodate the dimensions of the electrode arrray within our computational limitations restricted the resolution of the simulation space. Because of this resolution limitation each retinal layer was represented by only 1-2 voxels of thickness. This necessarily led to distortion of the thicknesses because the discrete increment by which the thicknesses could be adjusted was large relative to the feature size. The final total retinal thickness was 249.6 μm (8 voxels at 31.2 μm per voxel.) This is within one voxel width of the 261 μm average retinal thickness of organ donors aged 66 years and older reported by Cavalotti et al. [5] The 31.2 μm resolution limit required the merging

of the smallest layer, the outer plexiform layer, and the adjacent fiber layer. Because the fiber layer is more resistive than the outer plexiform layer, the resistivity of the fiber layer was used. Figure 4.8(b) shows the final retinal model in detail, and Table 4.2 lists the resistivity and thickness of each layer in the model.

Table 4.2: Resistivity Values ($\rho = 1/\sigma$) and Thicknesses of Retinal Tissues Used for Simulation

material	ρ (Ω·m)	thickness (μm)
photoreceptors	50.500	62.4
outer nuclear layer	60.000	31.2
fiber layer/outer plexiform layer	70.00	62.4
inner nuclear layer	65.00	31.2
inner plexiform layer	18.00	31.2
ganglion cell layer	70.00	31.2
optic fiber layer	70.00	31.2

4.2.3 Current Spread for Epi-Retinal and Trans-Retinal Electrode Configurations

Figures 4.10 through 4.15 are visualizations of the current intensity data. Color intensity plots are used because they give an intuitive understanding of the current distribution. Then numerical data is presented to allow comparison of current density values in the ganglion cell layer due to the two electrode configurations.

Figure 4.10 shows cross-sectional current intensity data from the epi-retinal configuration shown in Figure 4.6(a). Looking closely at the cell layers in close proximity to the electrode array, it can be seen that there is a significant level of variation in current intensity. These types of peaks and valleys are the kind of variation necessary for appropriate retinal stimulation. Also note that there is a general rise in current density

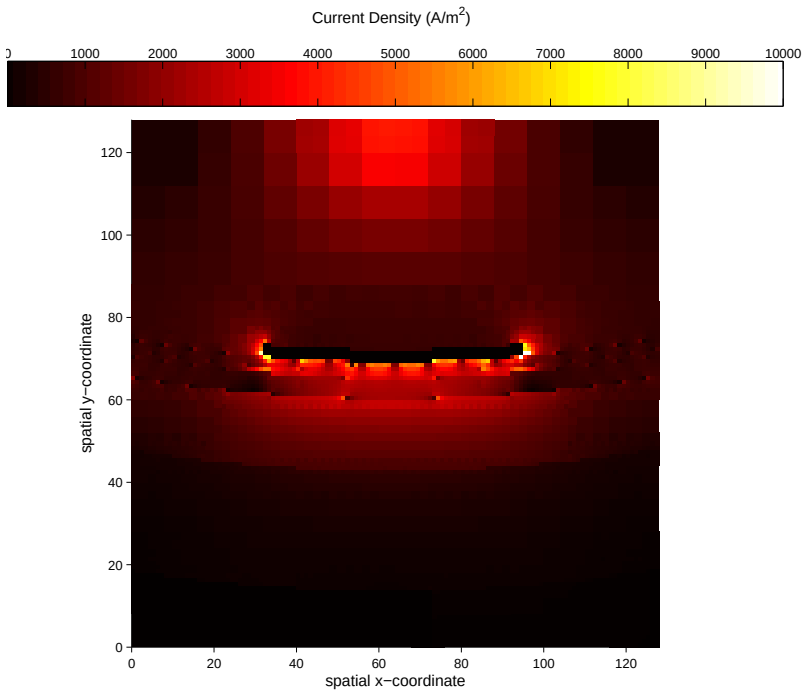

Figure 4.10: Cross-sectional current intensity plot of epi-retinal electrode configuration. Maximum current density found was 27,000 A/m^2

towards the top of the diagram, as current converges toward the return electrode.

Figure 4.11 shows cross-sectional current densities from within the ganglion cell layer. The plane of data points portrayed here would lie perpendicular to the plane of Figure 4.10. In this plot the pattern of the electrode array is clearly visible. Because the current distribution still reflects the layout of the electrode array, we can conclude that there is promise for stimulating the ganglion cells by use of an epi-retinal array. Figure 4.12 gives an indication of the current spread at the boundary between the choroid and retina (the layer of the retina furthest way from the electrode array.) The general location of the electrode array is clearly evident, but it is difficult to distinguish the location of the individual electrodes from this plot, indicating that by the time the current stimulus reaches the opposite edge of the retina, the current density pattern has degraded

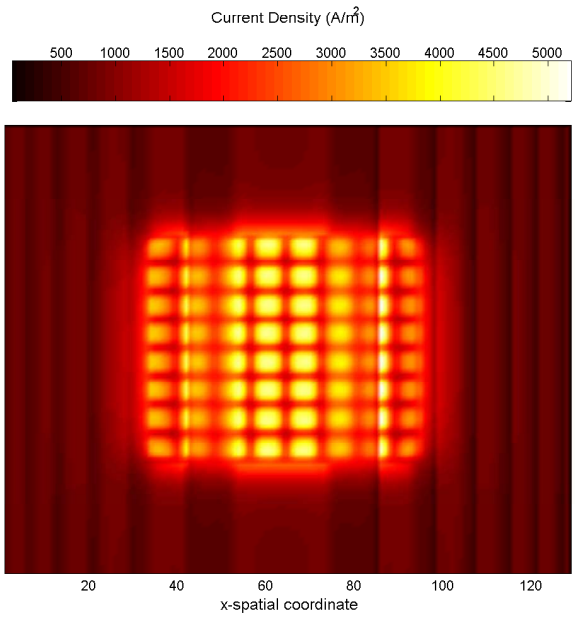

Figure 4.11: Cross-sectional view of current density within the ganglion cell layer.

significantly within this relatively small distance.

Figure 4.13 shows the current spread in the same trans-retinal cross-section shown in Figure 4.8(a). This configuration produces a low and uniform current density in the retinal layer of interest. Figures 4.14 and 4.15 refer to planes parallel to the electrode array that show the current density within particular layers of the retina. Figure 4.14 shows the ganglion cell layer that we wish to stimulate. From this image we can see a fairly flat, uniform intensity. This suggests that this trans-retinal electrode array is probably not a viable configuration. Figure 4.16 confirms this conclusion. The upper line indicates the current density induced in the epi-retinal array. In this data the current density minima and maxima differ by approximately 50%. In the trans-retinal data, shown in the lower data set, shows no discernable variation that would correspond to the

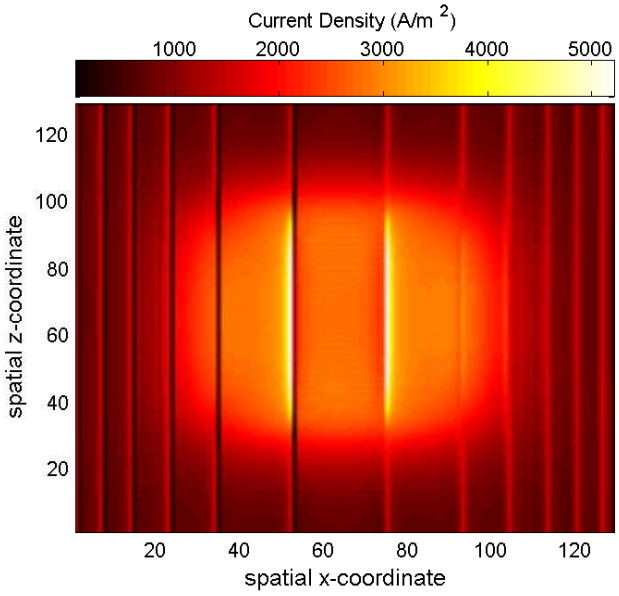

Figure 4.12: Current intensity at retinal layer furthest from the electrode array.

electrode pattern.

From Figure 4.16 it is apparent that the average current density levels seen in the target ganglion cells are greater for the epi-retinal configuration than for the trans-retinal. This is effectively equivalent to observing that the current levels in the ganglion cell layer are more uniform due to current spreading and dissipating more evenly across the tissues. Because the total injected current for both simulations was equivalent, this plot does make it clear that even if some effective current steering were possible with trans-retinal electrodes, the amount of dissipation would likely require higher overall injected current levels. This would require more power dissipation in the eye tissue, something that should be minimized due to safety considerations.

The results of these simulations indicate that the trans-retinal electrode configuration offer little promise for providing an effective current steering solution for retinal

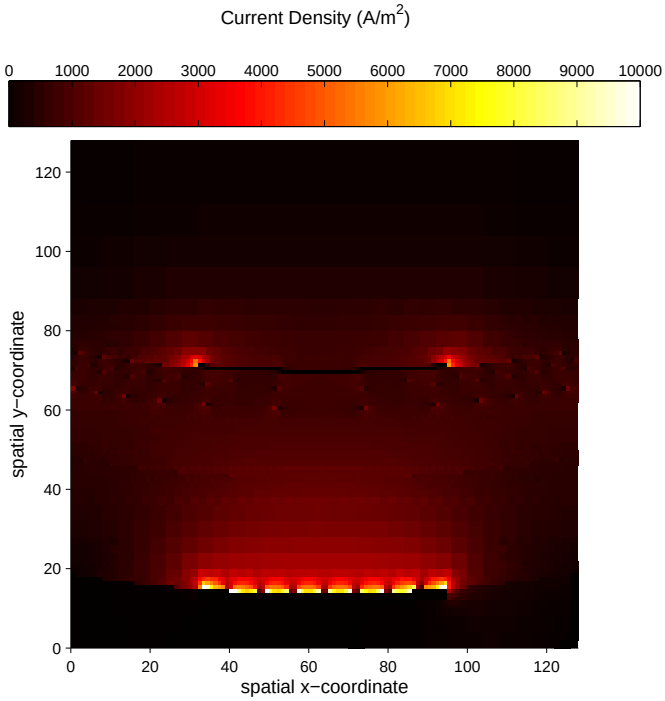

Figure 4.13: Cross-sectional current intensity plot of trans-retinal electrode configuration. Maximum observed current density was 17,000 A/m^2.

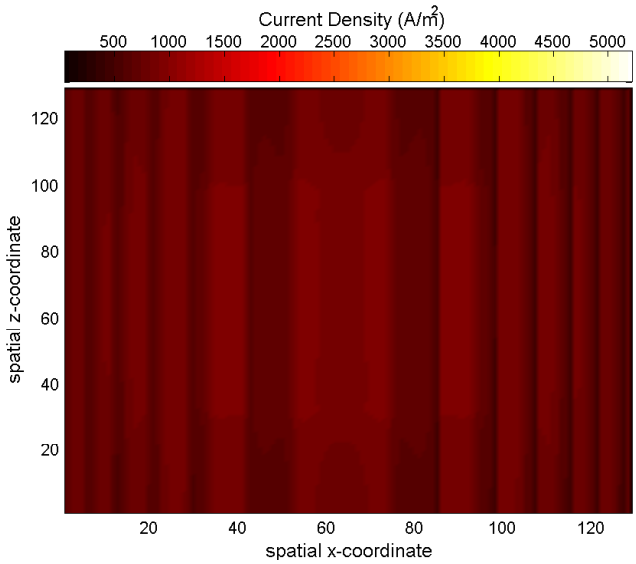

Figure 4.14: Current intensities in plane of the ganglion cell layer induced by trans-retinal stimulation.

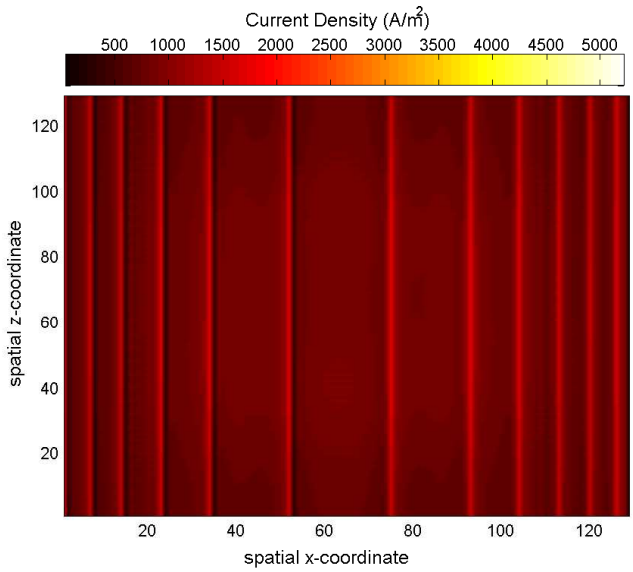

Figure 4.15: Current intensities induced by trans-retinal stimulation in plane of the photoreceptor layer adjacent to the choroid.

stimulation. The epi-retinal configuration offers greater promise because it generates a discernable pattern in the ganglion cell layer. This result was ultimately expected, but the degree of effectiveness of the trans-retinal configuration needed to be assessed in order to determine if it should be considered as an option. These simulation results indicate that it is not a realistic solution.

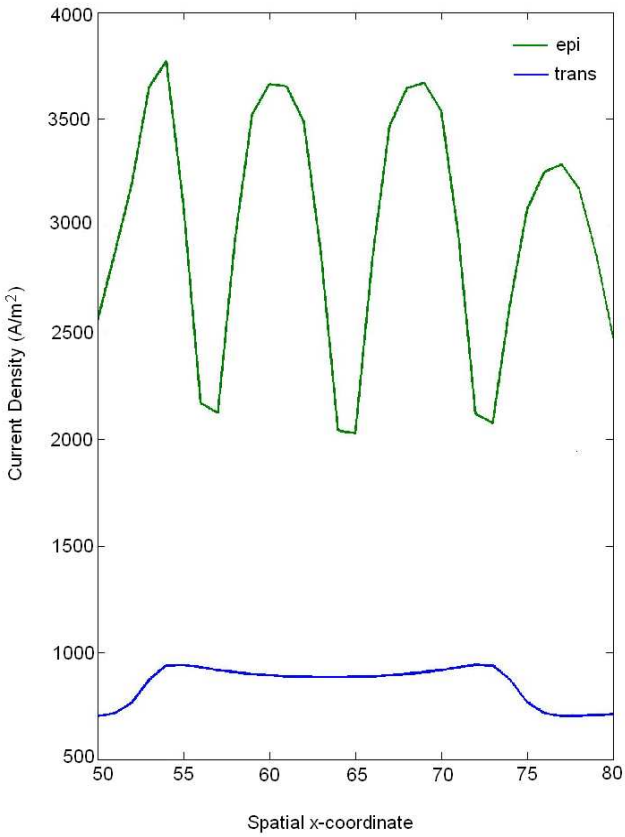

Figure 4.16: Current Density points within the ganglion cell layer laying directly in front of the stimulating electrode arrays. The upper and lower data sets are from the epi-retinal array and trans-retinal arrays respectively.

Chapter 5

Two-Dimensional Simulation Results

Two-dimensional approximations can be useful for situations in which large size or high resolution of the simulation space makes three-dimensional simulations impractical. For these reasons and because it was available before the three-dimensional simulator was completed, a two-dimensional impedance method code originally written by Eberdt [13] was applied to retinal prosthesis problems. In order to be applied to our simulations, Eberdt's method was heavily modified to include current source stimuli because in its original form, only magnetic stimuli were accommodated. The multi-resolution capabilities and data structure from this code were kept, and the extra functionalities were built on top of the foundation laid down by Eberdt.

In this chapter we first investigate the retinal current spread characteristics of coaxial electrodes. The current densities induced in the ganglion cell layer by differently sized coaxial electrodes are evaluated and emerging trends are analyzed. Second, the influence of an imperfect electrode-retina interface is considered by displacing an electrode array away from the retina by a single voxel width. These results are then compared with those

of a model identical in all ways except that the electrodes make perfect contact with the retinal surface

5.1 Investigation of Coaxial Electrode Configurations with High Resolution Classified Retina

For a retinal prosthesis to function properly, it is necessary to design electrodes such that only a select region of tissue within a close proximity is stimulated when the electrode injects current. Because all current must sink at a return point, the location of this current return has as much affect on the overall current path as the location of the source electrodes. In the three dimensional electrode configurations that were tested in chapter 4, the current return point was treated as a single electrode because recent retinal prosthesis prototypes function in this manner. However, because the objective is to stimulate only a localized area within a close proximity of each electrode, it would be advantageous if each electrode could have a nearby, dedicated current return. An array of coaxial electrodes would elegantly offer this type of functionality. To investigate the use of coaxial configurations, coaxial electrodes with varying physical dimensions were simulated using the two-dimensional multi-resolution code in order to determine how current penetration characteristics are influenced by electrode dimensions.

A cylindrical coaxial electrode configuration would consist of an inner conductive disk and a surrounding concentric circular conductor. The physical dimensions of this electrode can be defined by three distinct radii: that of the inner disk, the radius to the

inner edge of the outer conductor, and the radius to the outer edge of the outer conductor. In the two-dimensional approximation a coaxial configuration would be represented by a central flat conductor and two flat outer conductors. The contact surfaces of these structures are shown in Figure 5.1.

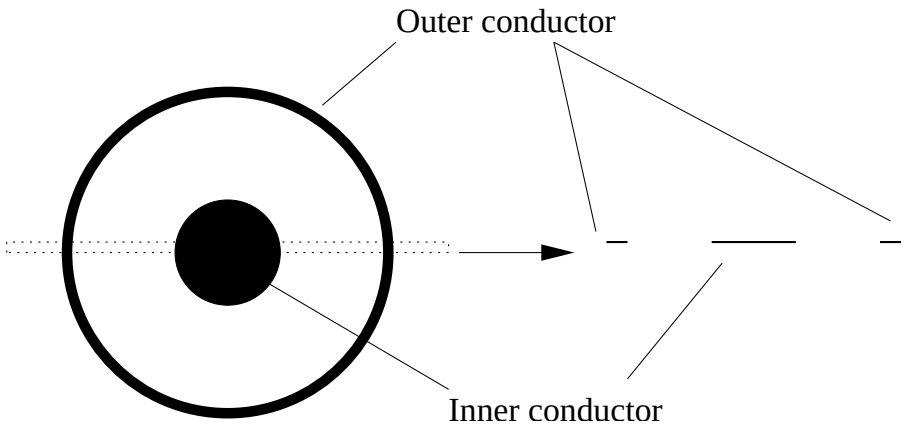

Figure 5.1: Contact surface of three-dimensional structure of coaxial electrode (left.) Approximation of coaxial structure used for two-dimensional simulations (right.)

Twelve different coaxial electrodes were simulated, four variations on electrodes with three different total widths of the outer conductor: 50, 100, and 150 μm. The inner conductors were sized so that the ratios of inner to outer electrode radii were 1/10, 3/10, 5/10, and 7/10. The electrodes were tested with a detailed retinal model constructed from an SEM image of a stained retinal cross section taken from Rodieck et al. [21] Model resolution was 0.454 μm. As with the three-dimensional simulations, the electrical properties of the retinal layers were taken from Karwoski. [20] Each electrode was positioned on the inner surface of the retina against the inner limiting membrane, in an epi-retinal configuration as shown in Figure 5.2. A total current of 600 μA was injected through the central electrode and the outer conductor served as ground (current return.)

Current intensity plots for the 100 μm electrode size are shown in Figure 5.3. As

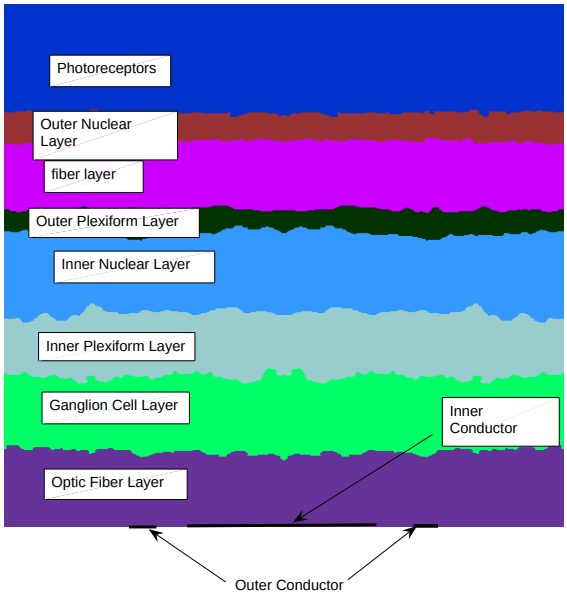

Figure 5.2: Classified retina model used for coaxial electrode simulations. Model was based on SEM image of stained retinal cross-section presented by Rodieck. [21]

Table 5.1: Resistivity Values of Retinal Tissues ($\rho = 1/\sigma$)

material	ρ (Ω·m)
photoreceptors	50.500
outer nuclear layer	60.000
fiber layer	18.000
outer plexiform layer	18.20
inner nuclear layer	65.00
inner plexiform layer	18.00
ganglion cell layer	70.00
optic fiber layer	70.00

expected, most of the current tends to be confined around the coaxial electrode, and current levels in the ganglion cell layer are small in comparison. However, even though the overall current density levels in the ganglion cell layer were generally low, they follow a consistent pattern in relation to the total width of the electrode and the ratio of the inner to outer conductor widths. Figure 5.4 shows the maximum current density generated within the central portion of the ganglion cell layer plotted against the ratio

of inner to outer conductor widths for the 50 μm electrode size. The discrete points indicate the calculated current densities, and the continuous line is the least squares fit of these points for a second degree polynomial.

Figure 5.5 shows these best-fit curves for all three electrode sizes plotted on the same axis. Three characteristics of this graph are immediately apparent. First, the overall ganglion cell layer current density is consistently higher for the larger electrode sizes. Second, the rate of decrease in current density is greater for the larger electrode sizes. And third, as can be seen by observing polynomial graph and the polynomial coefficients, the second degree term becomes weaker as total electrode width increases. A strong quadratic component is apparent in the 50 μm polynomial, and the 150 μm polynomial appears highly linear. The size between the two, 100 μm has an intermediate shape.

Table 5.2: Coefficients for 2nd Degree Best-Fit Ganglion Cell Current Density Polynomials

width	r^2	r	1
$50\mu m$	-0.8350	0.2003	0.4860
$100\mu m$	-0.8944	-0.3875	1.4062
$150\mu m$	-0.1875	-1.2768	1.8435

5.2 Current Leakage Due to Imperfect Electrode-Retina Contact

In our discrete models, it is assumed that each voxel is completely filled by a single type of material and that these material properties are completely representative of the entire volume occupied by that voxel. One deficiency of this approach to modeling is the

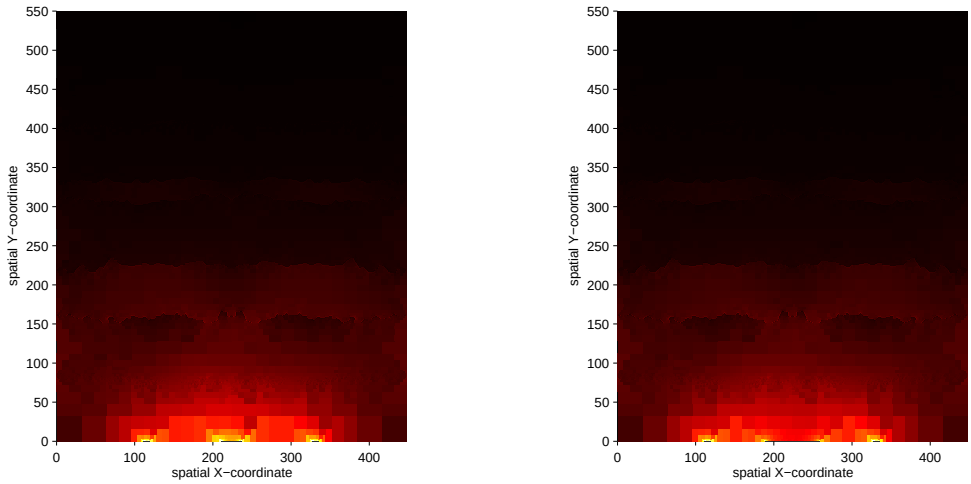

(a)

(b)

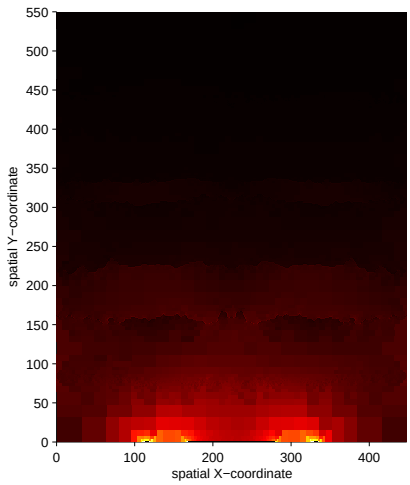

(c)

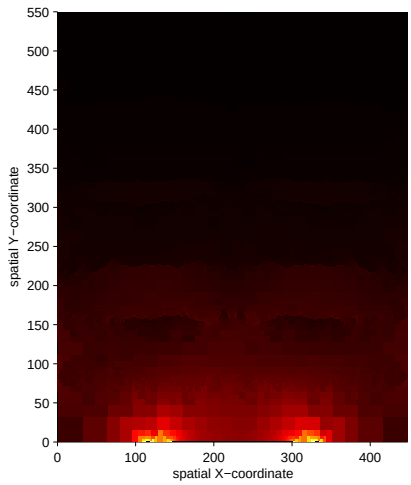

(d)

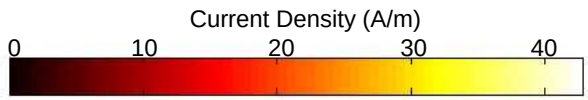

(e)

Figure 5.3: Current intensity plots for simulation of coaxial electrodes with total width of 100 μm. The ratio of inner electrode widths to outer electrode widths are 1/10 (a), 3/10 (b), 5/10 (c), and 7/10 (d). The colorbar indicating current densities is shown in (e).

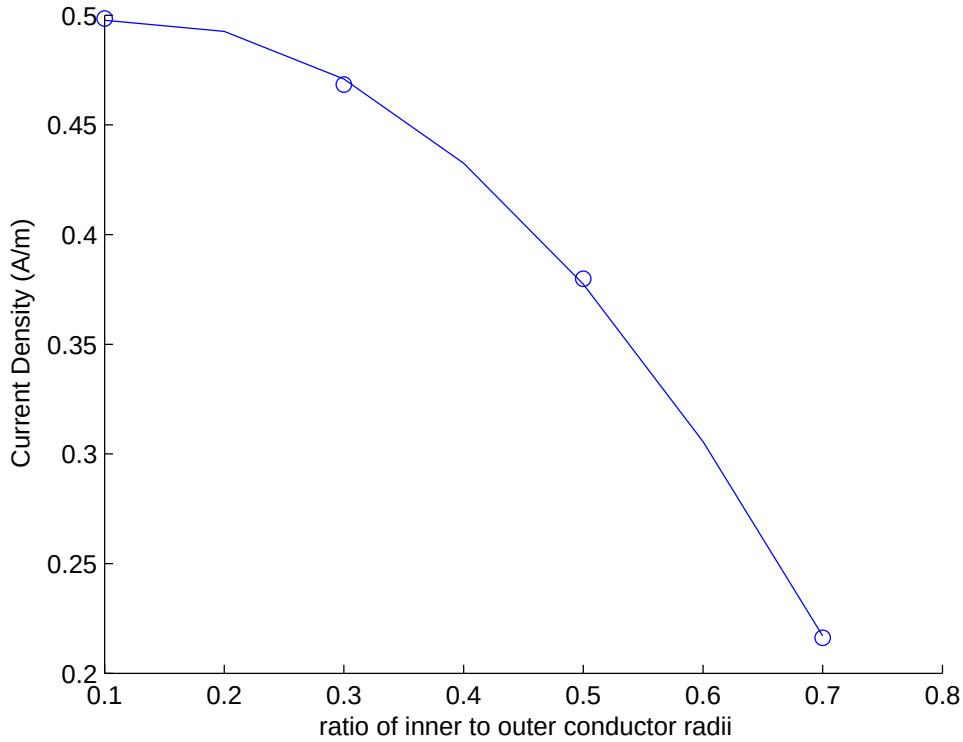

Figure 5.4: Maximum current density generated in the ganglion cell layer by plotted against the ratio of the inner and outer conductor radii with best fit 2nd degree polynomial. Total electrode width was 50 μm.

difficulty of accounting for characteristics of features that do not occupy a volume, such as the characteristics of an interface between two voxels of differing materials. In our admittance method simulations, this has the potential to become particularly problematic at the interface between the electrode array and the retina. Figure 5.7 shows a close view of the electrode-retina interfaces for an epi-retinal electrode array. Each electrode is embedded in a perfect insulator, so that its only electrical connections are directly with retinal tissue. This is unrealistic because the contact would likely be imperfect. This could be significant because the conductivity of the retina (average $\sigma = 0.02$ S/m) [20] is lower than the resistivity of the vitreous humor that fills the eyeball ($\sigma = 1.5$ S/m.) [15] In

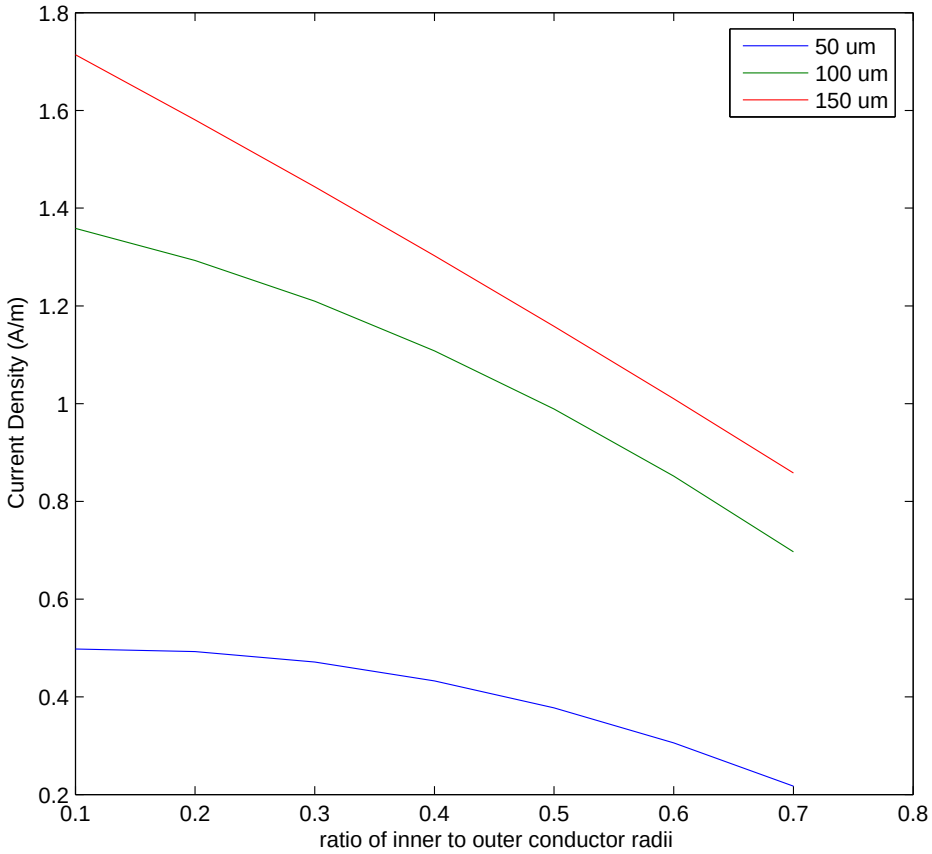

Figure 5.5: Second degree best fit polynomials for the maximum ganglion cell layer current density as a function of conductor radii for the three tested electrode widths.

the case of imperfect contact, a small amount of this highly conductive fluid could present a path of significantly less resistance from the electrode to the current return. In essence this could provide an imperfect "short circuit" between the firing electrode and ground. This phenomenon has the potential to seriously impact the validity of simulation results. In order to assess this possibility, simulations were run that compared two identical electrode arrays, one with perfect contact with the retina, and one which made imperfect contact.

Figure 5.7 shows a closeup view of the models used to test both connections. As

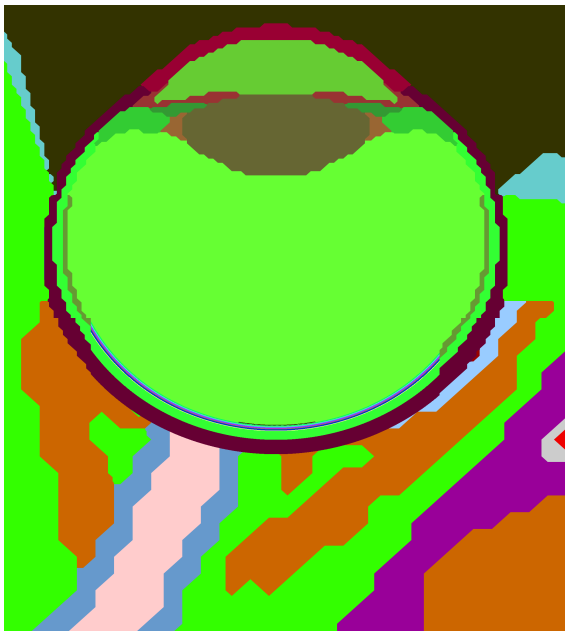

Figure 5.6: Entire model used for simulation of perfect and imperfect electrode contact.

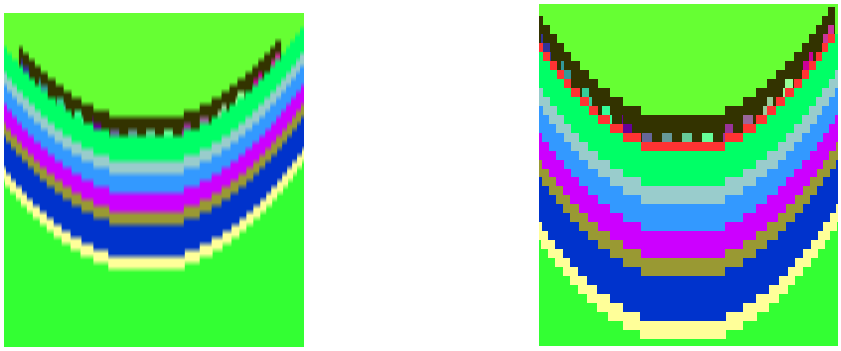

(a) (b)

Figure 5.7: Models used to test influence of conductive gap. The model without the conductive gap is shown in (a) and the model including conductive gap is shown in (b). The conductive gap is shown by the red cells in (b) and have the same material properties as vitreous humor.

mentioned before, the admittance method had no way of accounting for the interface, so to artificially create imperfect contact, the electrode array was displaced from the retina by inserting a single voxel layer of material with the same electrical properties as vitreous humor between the electrodes and the retina. This can be seen in Figure 5.7(b) as the layer of red cells separating the electrode array from the retinal layers. Because an entire voxel with an actual volume is used to simulate what would be a relatively flat interface, this implementation would likely over-estimate the amount of current leakage caused by imperfect isolation. However, we use both of these extreme cases to determine potential best-case and worst-case scenarios, and then assess the significance of the discrepancy.

The model used for these simulations is essentially a cross-section of the hybrid model described in chapter 4, section 4.2.2. However, the model in these simulations used a finer resolution of 15.6 μm rather than 31.2 μm. Similar problems were encountered when trying to obtain the most accurate thicknesses of the retinal layers because the 15.6 μm resolution is still large compared to the feature sizes. Table 5.4 lists the actual thicknesses and resistivities of the retinal layers used in our model, and Figure 5.8 shows a cross-section of this model. Table 5.3 shows the resistivities used for non-retinal tissues. Layer thicknesses were selected to reflect the proportions from Rodieck [21], retinal resistivities were taken from Karwoski et al. [20], and non-retinal tissue resistivities were obtained from Gabriel et al. [15]

Simulations were run using a two-dimensional model of the entire ocular orbit, with the current return placed both inside and outside of the eye. The return location within the eye was on the retinal surface, but significantly removed from electrode array. The return location located outside of the eye was inserted against the sclera in the nasal

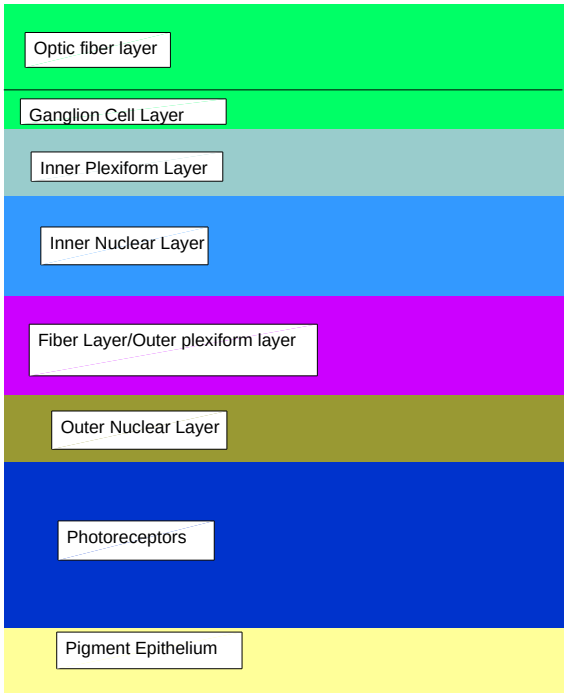

Figure 5.8: Model of retina used for conductive gap simulations. Layer thickness and resistivity are given in Table 5.4.

Table 5.3: Resistivity Values of Non-Retinal Tissues ($\rho = 1/\sigma$)

material	ρ (Ω·m)
post chamber	0.666
ciliary muscle	4.130
choroid	1.080
sclera	1.98
aqueous humor	0.666
vitreous humor	0.666
cornea	2.371
pupillary muscle	4.130
lens	3.108
fat	50.000
generic muscle	4.130
bone	50.000

Table 5.4: Resistivity Values ($\rho = 1/\sigma$) and Thicknesses of Retinal Tissues Used for Conductive Gap Simulations

material	ρ (Ω·m)	thickness (μm)
photoreceptors	50.500	62.4
outer nuclear layer	60.000	31.2
fiber layer/outer plexiform layer	70.00	46.8
inner nuclear layer	65.00	46.8
inner plexiform layer	18.00	31.2
ganglion cell layer	70.00	31.2
optic fiber layer	70.00	31.2
pigment epithelium	3200	15.6

region. In these simulations, the location of the current return did not induce significant differences in the current spread. Therefore, to avoid redundancy the results for only the nasally located current return simulations are presented.

Figure 5.9 shows calculated current densities for the entire simulation space. The electrode array and the current return, located at the bottom of the eye and to the upper left respectively, are clearly visible as current densities are high at these locations. Figure 5.10(b) shows the current intensities in the tissues within close proximity of the electrode arrays. From this comparison we can observe that there are generally higher current density levels within the retinal layers. Figure 5.11 shows a plot of the current density levels in the ganglion cell layer. The coordinate of the horizontal axis in this plot corresponds with the horizontal axis in Figures 5.7. The upper line indicates the current densities found from simulations with no spacing between the electrodes and retina, and the lower with the exaggerated spacing introduced.

As expected, current densities in the case of a perfect interface between the electrode and retina were higher than those from the imperfect connection. Interestingly, the current densities in the very middle of the electrode array were nearly equivalent for

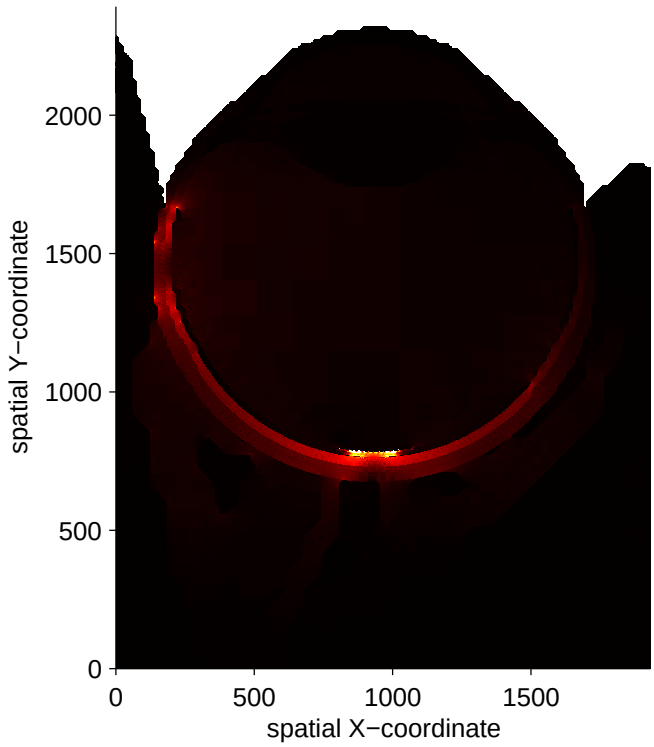

(a)

(b)

Figure 5.9: Current intensity plot for entire simulation space of model without the conductive gap. Maximum observed current density 0.97 A/m.

both cases. The differences grow to a maximum at the electrodes located at the edges of the array. This result can be explained by the conductive gap between the electrode and retina. As current emerges from the electrodes, it will have a tendency to move towards the current return. This results in some of the current moving in a lateral direction, along the retinal layers rather than perpendicularly through them. Therefore, as currents from the central electrodes move toward the edges of the array, the currents accumulate,

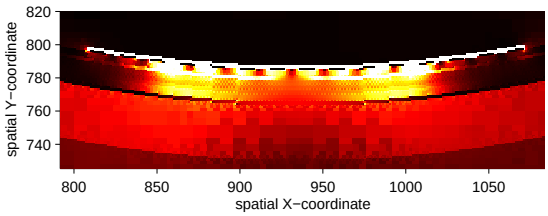

(a)

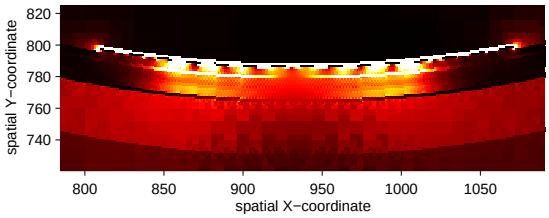

(b)

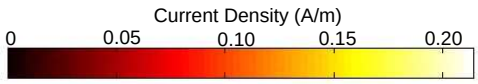

(c)

Figure 5.10: Current intensity plots of models including without the conductive gap (a) and the with (b) the conductive gap. The current density color scale is shown in (c). Maximum current densities observed for the simulations without and with the conductive gap were 0.97 A/m and 1.75 A/m respectively.

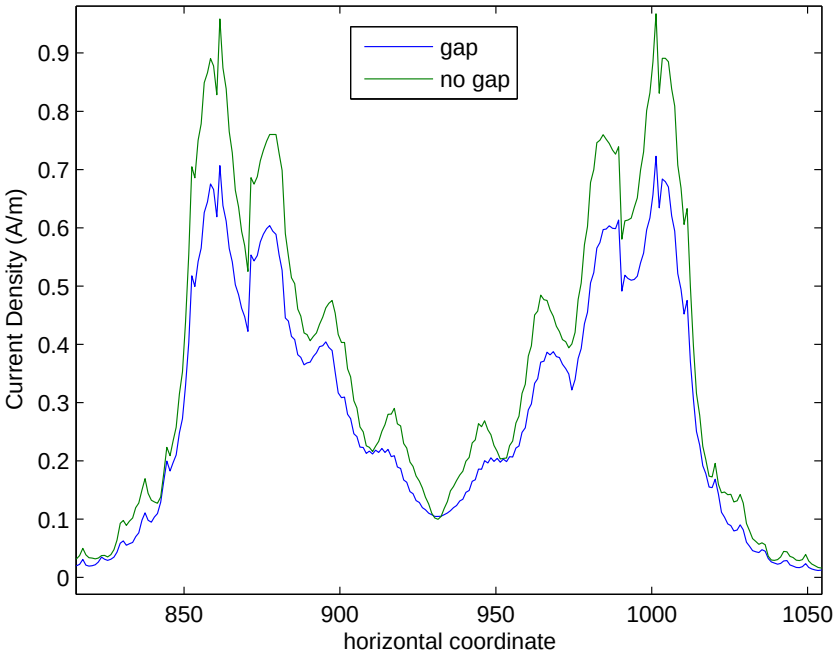

Figure 5.11: Current Densities in Ganglion Cell Layer directly in front of electrode array.

resulting in the incrementally increasing characteristic observed in Figure 5.11.

The results in Figure 5.11 show that the current density levels are significantly affected by the presence of the conductive channel. However, the overall shape of the curve was consistent. The maximum current density discrepancy 27% is observed between the two models.

Chapter 6

Conclusions and Future Directions

A three-dimensional multi-resolution admittance method has been developed, tested, and shown to be capable of reducing cell counts by over 50% while maintaining a high level of accuracy. The method was used to investigate the properties of electrode configurations situated in anatomically realistic models of the ocular orbit. These simulations indicated that the epi-retinal electrode array which places the electrodes against the retinal surface is a viable candidate for precise ganglion cell stimulation. The trans-retinal electrode array, in which the electrodes were placed outside of the eye, against the sclera, was shown to not be a suitable solution.

Two-dimensional simulations were used to determine current spread characteristics of coaxial electrodes. A gradual transition from a quadratic to linear relationship between current density induced in the retina and electrode size was observed as total electrode width was increased. Furthermore, two-dimensional simulations were used to estimate the influence of imperfect retina-electrode contact for epi-retinal electrodes by placing a conductive channel between two surfaces. This channel was found to significantly affect

the current penetration into the target ganglion cell layer. The general shape of the current patterns was found to be similar, but the current densities were reduced between 0-27% in the model with the conductive gap.

As suggested by the influence of the conductive channel, one of the most needed additions to our method would be a way of characterizing interfaces between two materials. This would allow us to model imperfect electrical contacts between materials. Also, it would also allow us to model the phenomena of contact capacitance that can occur when an electrode generating an AC potential interfaces with a conductive solution. Because body tissues consist primarily of water, this capacitance is likely a significant consideration for retinal prosthesis simulations.

In order to better understand the nature of how currents induce changes in neuron potentials, impedance method simulations could be applied to realistic models of neurons. This would allow us to observe the manner in which voltage changes across the neural membrane could be influenced by the shape, size and other physical characteristics of the neuron. This type of simulation mark a new microscopic level of modeling that would present new challenges for our impedance method because neurons are very structurally complex and exhibit highly non-linear electrical characteristics. Representation of this non-linear behavior would likely require extensive modification of our methods used to solve for potentials in the impedance mesh. In our current implementation, only static, unchanging linear models can be simulated. A natural method for simulating neural behavior would be to implement a time-stepping scheme that could account for the non-linear behavior of neural tissue.

With the development of non-linear models, the basic impedance method could serve

as a foundation on which to develop a biologically specialized modeling scheme. As layers of complexity and non-linearity are added to the scheme, the simulator could become a true physics based method of simulating complex bio-electrical phenomena.

Bibliography

[1] J.K. Chapin, K.A. Moxon. *Neural Prostheses for Restoration of Sensoy and Motor Function*, Boca Raton, Florida: CRC Press, 2001.

[2] Cochlear Implant Association, http://www.cici.org/, Accessed 2004 November.

[3] N.A. Campbell, J.B. Reece, L.G. Mitchell. *Biology*. Menlo Park, CA: Benjamin/Cummings, Addison Wesley Longman, 1999.

[4] D. H. Liang, H. S. Lusted, and R. L. White. "The nerve-electrode interface of the cochlear implant: current spread," *IEEE Trans. on Biomedical Engineering*, 46(1):35–43, January, 1999.

[5] C. Cavallotti, M. Artico, N. Pescosolido, F.M. Tranquilli Leali, J. Feher. "Age-related changes in the human retina," *Canadian Journal of Ophthalmology*, vol. 39, no. 1, February 2004.

[6] S.I. Fox. *Human Physiology*, New York: McGraw-Hill, 2004.

[7] M. S. Humayun, E. de Juan Jr., J.D. Weiland, G. Dagnelie, S. Katona, R. J. Greenberg, S. Suzuki. "Pattern electrical stimulation of the human retina," *Vision Research*, 39:2569–2576, 1999.

[8] *IEEE Standard for Safety Levels with Respect to Human Exposure to radio Frequency Electromagnetic Fields, 3 kHz to 300 GHz*, IEEE Standard C95.1-1999.

[9] D.W. Armitage, H.H. LeVeen, and R. Pethig. "Radiofrequency-indeuced hyperthermia: computer simulation of specific absorbtion ratio distributions in realistic anatomical models." *Physics in Medicine and Biology*, 28:31-42, 1983.

[10] O.P. Gandhi, J.F. DeFord, and H. Kanai. "Impedance method for calculation of of power deposition patterns in magnetically induced hyperthermia." *IEEE Transaction on Biomedical Engineering*, 31:644-51, 1984.

[11] R. Plonsey and R. Barr. *Bioelectricity, A Quantitative Approach*. New York: Kluwer Academic/Plenum Publishers, 2000.

[12] A.G. Leventhal, Ed, and J.R. Cronly-Dillon, Ed. *Vision and Visual Dysfunction vol. 4: The Neural Basis of Visual Function*. Boca Raton, FL: CRC Press, 1991.

[13] M. Eberdt. "A Multi-Resolution Meshing Scheme for the Impedance Method." Computer Science Master's Thesis, North Carolina State University, 2001.

[14] National Institute of Standards and Technology, http://math.nist.gov/iml++/, Last Accessed 2004 November.

[15] C. Gabriel and S. Gabriel. "Compilation of the Dielectric Properties of Body Tissues at RF and Microwave Frequencies", http://http://www.brooks.af.mil/AFRL/HED/hedr/reports/dielectric/home.html, Last Accessed 2004 November.

[16] H. Samet. *The Design and Analysis of Spatial Data Structures.* Addison-Wesley, Reading, MA, 1990.

[17] S. C. DeMarco, *The architecture, design and electromagnetic and thermal modeling of a retinal prosthesis to benefit the visually impaired.* Ph.D Dissertation, North Carolina State University, 2003.

[18] B. Dreher, Ed; S.R. Robinson, Ed. and J.R. Cronly-Dillon. *Vision and Visual Dysfunction vol. 3: Neuroanatomy of the Visual Pathways and Their Development.* Boca Raton, FL: CRC Press, 1991.

[19] The National Library of Medicine. The Visible Human Project. http://www.nlm.nih.gov/research/visible/visible_human.html, 2000.

[20] C.J. Karwoski, D.A. Frambach and L.M. Proenza. "Laminar Profile of Resistivity in Frog Retina." *Journal of Neurophysiology*, vol. 54, 1607-1619.

[21] R.W. Rodieck. "The Primate Retina." *Comp. Primate Biol.*, vol. 4, 203-278, 1988.